Submitted to *Physics of Fluids*

Direct numerical simulations of activation and deactivation in turbulent atmospheric clouds

Abdullah Al Muti Sharfuddin,[1] Foluso Ladeinde,[1,a)] Yangang Liu,[2] Mohammad Atif,[3] Fan Yang,[2] Vanessa Lopez-Marrero,[3] Meifeng Lin,[3] and Tao Zhang[2]

[1]*Department of Mechanical Engineering, 113 Light Engineering Building, Stony Brook University, 100 Nicolls Road, Stony Brook, New York, 11794-2300, USA*

[2]*Environmental and Climate Sciences Department, Brookhaven National Laboratory, 2 Center St, Upton, New York, 11973-5000, USA*

[3]*Computational Science Initiative, Brookhaven National Laboratory, 2 Center St, Upton, New York, 11973-5000, USA*

Significant knowledge gaps remain in our understanding of turbulence-cloud-aerosol interactions in the Earth's atmosphere, and direct numerical simulation (DNS) has increasingly become an indispensable tool to fill such critical knowledge gaps. This study is an extension of our previous DNS model [Z. Gao, Y. Liu, and X. Li, Journal of Geophysical Research: Atmospheres, 123 (4), 2194-2214 (2018)], with a focus on the activation of aerosol particles into cloud droplets and deactivation of cloud droplets into aerosol particles in a microscale cloud environment. The effects of turbulence intensity, particle curvature and solute, as well as the initial distributions of the aerosol particles (monodisperse or polydisperse) are investigated. The governing equations for the flow of air, temperature, and water vapor mixing ratio are solved in Eulerian fashion by use of a finite difference-based procedure, assuming homogeneous and isotropic turbulence. The dynamics of the aerosol and cloud particles are calculated with the Lagrangian particle tracking method. The results show that the deviations of the thermodynamic variables from their respective means are significantly reduced, and the deactivation process occurs more rapidly, as the turbulence intensity is increased. The inclusion of particle curvature and solute effects, as well as polydispersity, tends to retard the activation of aerosols into clouds. Our results also suggest that the activation and deactivation processes are mean-dominated with the possibility of fluctuation-influenced activation or deactivation for the parameters investigated.

[a)] Author to whom correspondence should be addressed. Electronic mail: Foluso.Ladeinde@Stonybrook.edu

NOMENCLATURE

α_T, α_c = thermal accommodation coefficient [-], mass accommodation coefficient [-]

c_p, C_d = specific heat of air [J/(kg.K)], rate of condensation or evaporation [1/s]

Da, δ_{k,k_f}, ϵ_{in} = Damkohler number [-], delta function [-], energy injection rate [m^2/s^3]

ϵ, η = turbulent kinetic energy dissipation rate [m^2/s^3], Kolmogorov length scale [m]

$\boldsymbol{F}_b$, $\boldsymbol{F}_c$, $\hat{\boldsymbol{f}}_c$ = buoyancy force [N], external force [N], external force in the Fourier space [N]

$\boldsymbol{g}$, $\boldsymbol{k}_f$ = acceleration vector due to gravity [m/s^2], forcing wavenumber vector [1/m]

k_{min}, k_{max} = minimum wavenumber [1/m], maximum wavenumber [1/m]

κ, k_T = hygroscopicity of solute [-], thermal conductivity in air [W/(m.K)]

L_h, λ, l = specific latent heat [J/kg], Taylor microscale [m], integral length scale [m]

M_l, M_a = molar mass of water [kg/mol], molar mass of air [kg/mol]

m_l, m_a = mass of liquid water per grid cell [kg], mass of air per grid cell [kg]

μ_T, μ_v = molecular diffusivities [m^2/s] of temperature, water vapor

ν, p = kinematic viscosity of air [m^2/s], instantaneous fluid pressure [N/m^2]

p_{sat}, q_c = saturation water vapor pressure [N/m^2], instantaneous liquid water mixing ratio [g/kg]

q_v, $q_{v,s}$ = instantaneous water vapor mixing ratio [g/kg], saturation vapor mixing ratio [g/kg]

r_d, r = dry aerosol radius [μm], wet radius of aerosol particle or cloud droplet [μm]

r_c, R_v = critical radius [μm], specific gas constant for water vapor [J/(kg.K)]

R, $R_{w'w'}$ = universal gas constant [J/(kg.K)], autocorrelation coefficient [-]

ρ_a, ρ_l = density of air [kg/m^3], density of water [kg/m^3]

S_e, S_k = environmental supersaturation [-], particle equilibrium supersaturation [-]

S_c, σ_l = critical equilibrium supersaturation [-], surface tension of water [N/m]

T, τ_p = instantaneous temperature [K], particle response time [s]

τ_t, τ_c = turbulent mixing timescale [s], microphysical timescale [s]

$\boldsymbol{u}$, u_{rms} = instantaneous fluid velocity vector [m/s], root-mean-square velocity [m/s]

$\hat{\boldsymbol{u}}$, $\boldsymbol{V}$, $\boldsymbol{X}$ = Fourier velocity field [m/s], particle velocity vector [m/s], particle position vector [m]

PDF, TKE = probability density function [-], turbulent kinetic energy [m^2/s^2]

I. INTRODUCTION

In the Earth's atmosphere, aerosol particles grow and activate into cloud droplets in a supersaturated environment, while cloud droplets evaporate and deactivate into aerosol particles in a subsaturated environment. The growth of small particles and thus activation/deactivation rely on the competition between the curvature effect or Kelvin effect, and the solute effect or Raoult's law.[1] A spherical cloud droplet has a surface that is curved and consists of numerous water molecules. The greater the curvature, the greater the likelihood that water molecules will escape from the surface. This is the curvature effect, which favors evaporation compared to a flat surface. When solutes or dry aerosols are present, they occupy sites on the particle surface that would otherwise be occupied by water molecules. This is the solute effect[2] which prevents evaporation. Many studies have investigated the role of curvature and solute on activation and deactivation. For example, Yang et al.[3] studied the condensational growth of cloud droplets formed on polydisperse aerosol particles with the inclusion of curvature and solute effects, and Yang et al.[4] applied large-eddy simulation (LES) and Lagrangian microphysics to investigate activation and deactivation. They reported that the growth of haze or unactivated aerosol particles and cloud droplets have strong impact on cloud properties when supersaturation fluctuations are comparable to mean supersaturation. However, the LES approach does not resolve all scales of turbulence and thus requires approximate parametrizations. Korolev[5] showed analytically using a one-dimensional model that curvature and solute effects broaden droplet size spectra during condensation.

Atmospheric turbulence affects key cloud microphysical processes like condensation, evaporation, activation, and deactivation at the microscale.[6] When cloud droplets and aerosol particles are suspended in a turbulent environment, the mass and energy transfer between the moist air and dispersed phase (particles) becomes important. Grabowski et al.[7] studied the activation process in turbulent and non-turbulent cloud models and reported that all aerosol particles activate into cloud droplets in a non-turbulent setting but only a fraction of aerosol particles do so in a turbulent environment. On the other hand, Shawon et al.[8], who studied the dependence of aerosol-cloud interactions on turbulence in a laboratory setting, observed that turbulence causes more aerosol particles to be activated and that the activated fraction decreases monotonically as the aerosol number concentration increases. From a direct numerical simulation (DNS) study, Celani et al.[9] examined the role of turbulence in the growth process of cloud droplets, and reported turbulence-induced spectral broadening. They introduced the concept of the equivalent cloud condensation nuclei (CCN) as a way to signify the importance of turbulence in the process of cloud growth. Ditas et al.[10] measured the fluctuations in environmental supersaturation in a turbulent stratocumulus cloud layer and found that the

fluctuations decrease with increasing liquid water content and droplet number concentration. The authors also estimated the fluctuations in the temperature and vertical velocity, as well as the number fraction of activated aerosol particles. Thomas et al.[11] used DNS to investigate the condensational growth and activation of aerosol particles in response to fluctuations in the environmental supersaturation resulting from turbulence. They found that aerosol particles activate in small amounts until a maximum activation is reached and larger cloud droplets co-exist with smaller unactivated aerosol particles, also known as haze particles. An interesting investigation by Prabhakaran et al.[12] identified three regimes of aerosol activation from their experimental and theoretical study: mean-dominated, fluctuation-influenced, and fluctuation-dominated. The authors found that turbulence tends to deactivate cloud droplets and suppress aerosol activation in the mean-dominated regime. Only one-dimensional spatial models were used in this study.

Despite recent progress, as summarized in the foregoing, significant knowledge gaps exist in our understanding of the activation and deactivation processes in turbulent clouds. For example, the effects of the initial aerosol size distributions on activation and deactivation in a turbulent cloud environment has received little attention. Although the role of turbulent fluctuations on activation has been reported,[7,8,9,11,12] a systematic study of the impact of a range of turbulence levels on activation and deactivation is required. Moreover, previous investigations have limitations, including one-dimensional analysis, approximate analyses, or the limitations associated with the use of large-eddy simulation approach. The objective of this study is to investigate these aspects of activation and deactivation with a particle-based DNS model. The study involves solving a temporal and three-dimensional spatial model of the continuum phase by use of the DNS approach wherein all the scales of flow are resolved. The turbulence in our model is assumed to be homogeneous and isotropic,[13] which allows us to use spatial averaging for the statistics. The Lagrangian approach is used to track the motion and growth of particles. The DNS model developed by Gao et al.[14] is extended in the present work to incorporate the activation/deactivation processes as described by the kappa-Kohler theory.[15] We vary dry aerosol size distributions from monodisperse to polydisperse and generate different levels of turbulent kinetic energy (TKE) dissipation rate. The temporal growth and properties of aerosol particles and cloud droplets, along with the evolution of the thermodynamic fields of temperature and water vapor mixing ratio are investigated.

In the next section we present the governing equations for the dynamics and thermodynamics of the problem, as well as the models employed to describe the cloud droplets, including the curvature and solute effects. We then

summarize the numerical procedure employed in this study and list the relevant parameters. This is followed by the presentation of the results, with concluding remarks at the end of the paper.

II. GOVERNING EQUATIONS

The equations solved are described in this section. They include the Navier-Stokes equations, which express the conservation of momentum in the continuous phase (air). We also solve the transport equations for the thermodynamic variables, and the equations expressing the conservation of momentum for aerosols and clouds.

A. Turbulent velocity field

The turbulent air in the atmosphere is assumed to be governed by the physical-space Navier-Stokes equations with the Boussinesq approximation:[16]

$$\frac{\partial \boldsymbol{u}}{\partial t} + (\boldsymbol{u}.\nabla)\boldsymbol{u} = -\frac{1}{\rho_a}\nabla p + \nu\nabla^2\boldsymbol{u} + \boldsymbol{F}_b + \boldsymbol{F}_c\,, \tag{1}$$

$$\nabla.\boldsymbol{u} = 0\,. \tag{2}$$

Here, $\boldsymbol{u}$ is the instantaneous fluid velocity vector and p is the instantaneous fluid pressure. The terms in Eq. (1) are, in order, the time rate of change of velocity at a fixed point, the convective transport of momentum, the pressure force, the molecular dissipation of momentum, the buoyancy force, and the external force that is applied to sustain turbulence. Equation (2) is a statement of mass conservation for an incompressible flow, for which the density is constant with respect to space and time. The body force term $\boldsymbol{F}_b$ can be expressed as:[16]

$$\boldsymbol{F}_b = -\boldsymbol{g}\left[\frac{T - T_o}{T_o} + 0.608(q_v - q_{vo}) - q_c\right], \tag{3}$$

where T is the instantaneous temperature, T_o is the domain average of T, q_v and q_c are the instantaneous water vapor mixing ratio and liquid water mixing ratio, respectively, and q_{vo} is the domain average of q_v.

Although the gravitational body force term $\boldsymbol{F}_b$ could in principle maintain turbulence in the flow, the spatial dimensions (0.512 m in our model) involved in microscale physics is too small to permit a sustaining turbulence field. Thus, without turbulence production from shear, Dirichlet boundaries, or by baroclinic means, no natural mechanism is available in our model to prevent a complete decay of the imposed initial turbulence field. Thus, we introduce the external forcing term $\boldsymbol{F}_c$ in Eq. (1). The force is formulated in the Fourier space as:[17]

$$\hat{\boldsymbol{f}}_c(\boldsymbol{k}, t) = \epsilon_{in}\frac{\hat{\boldsymbol{u}}(\boldsymbol{k}, t)}{\sum_{k_f \epsilon_k}\left|\hat{\boldsymbol{u}}(\boldsymbol{k}_f, t)\right|^2}\delta_{k,k_f}\,. \tag{4}$$

where ϵ_{in} is an input TKE dissipation rate, $\boldsymbol{k}$ is the wavenumber vector, $\hat{\boldsymbol{u}}(\boldsymbol{k},t)$ is the Fourier-transformed velocity field, $\boldsymbol{k}_f$ is chosen from a wavenumber shell, and δ_{k,k_f} is a delta function. $\hat{\boldsymbol{f}}_c$ is inverse transformed into the physical space as $\boldsymbol{F}_c$ and used in our Navier-Stokes solver. Consistent with the Kolmogorov cascade theory of turbulence,[13] the low wavenumber end of the turbulence energy spectrum is forced.[18] The idea is that while the large scales of flow will be affected to some extent by forcing, the dynamics of the small scales are invariant, which emphasizes the need to localize the forcing within the low wavenumber end of the energy spectra. One could in principle vary the values of ϵ_{in} for the purpose of generating different turbulence intensities (TKE dissipation rates). However, preliminary work from the present study has shown a weak effect of ϵ_{in} when we transform the $\hat{\boldsymbol{f}}_c$ to the physical space, making it difficult to generate turbulence intensities that are significantly different. We have therefore chosen to use different bands of wavenumber forcing to generate the four levels of turbulence intensities (dissipation rates) that we investigate in this paper. We refer to these as 'very high', 'high', 'medium', and 'low' levels of turbulence. The abbreviations "V", "H", "M", and "L" are used respectively for these turbulence levels. The statistics for the four turbulence levels are provided in Table I. More details on the turbulence forcing are provided in Appendix A.

B. Thermodynamic variables

The thermodynamic variables of temperature, water vapor mixing ratio, and supersaturation need to be calculated alongside the flow velocity. The equations for temperature and water vapor mixing ratio are written in the Eulerian framework as:[14]

$$\frac{\partial T}{\partial t} + (\boldsymbol{u}.\nabla)T = \frac{L_h}{c_p}C_d + \mu_T \nabla^2 T\,, \tag{5}$$

$$\frac{\partial q_v}{\partial t} + (\boldsymbol{u}.\nabla)q_v = -C_d + \mu_v \nabla^2 q_v\,. \tag{6}$$

where C_d is the rate of mass exchange between liquid water and water vapor and is defined below in Eq. (16). The terms in Eq. (5) are, in order, the time rate of change of temperature at a fixed point, the convective transport of heat, the latent heat, and the molecular diffusion of heat. Equation (6) can be explained similarly. The equation set in (5) and (6) should be contrasted with those in one of the earlier studies of this problem.[19] In the latter, the base solutions correspond to the constant density, hydrostatic conditions in the atmosphere. The fluctuating fields were generated by perturbing the base conditions. The combined field (mean plus fluctuating) is solved in our approach. Thus, whereas the mean thermodynamic fields were contained in the base solutions in Ref. 19, they are combined with the fluctuating thermodynamic fields in our approach. Moreover, in our model, the mean values of the thermodynamic variables come

directly from the initial conditions. The convective terms in Eqs. (5) and (6) are of leading order and are of the same order as the local temporal change terms. However, they do not dissipate or augment the thermodynamic fields but merely transport the later from one point to another. Hence, the temperature and vapor mixing ratio fields are primarily passive tracers in our problem. Since we apply triply periodic boundary conditions in our studies (Sec. III A), there is no boundary layer behavior. Otherwise, the small magnitude of the diffusion terms (Tables IV and V) will lead to a (mathematically) stiff boundary layer behavior, which will make the specified initial value give way to the effects caused by a Dirichlet value at the wall, if one were specified. The absence of a no-slip condition coupled with the small magnitudes of the diffusion terms in our problem explains why the initial conditions for the thermodynamic variables serve as the mean values.

C. Description of aerosol particles and cloud droplets

The motion of each aerosol particle or cloud droplet is represented by the Lagrangian description, which consists of the kinematics of their motion and Newton's law. The simplified equations used can be written as[20]

$$\frac{d\boldsymbol{X}_i(t)}{dt} = \boldsymbol{V}_i(t)\,, \tag{7}$$

$$\frac{d\boldsymbol{V}_i(t)}{dt} = \frac{1}{\left(\tau_p\right)_i}\left[\boldsymbol{u}_i(\boldsymbol{X},t) - \boldsymbol{V}_i(t)\right] + \boldsymbol{g}\,. \tag{8}$$

where the subscript 'i' denotes the i-th aerosol particle or cloud droplet, $\boldsymbol{V}$ is its velocity vector, and $\boldsymbol{X}$ is its position vector. The terms in Eq. (8) denote, in order, the time rate of change of velocity, the Stokes drag force, and the gravitational force. The particle response time τ_p is given by[20]

$$\left(\tau_p\right)_i = \frac{2\rho_l r_i^2}{9\rho_a \nu}\,. \tag{9}$$

Equation (9) is valid for Stokes particles for which the Reynolds number based on the relative velocity between particle and bulk flow is significantly less than unity.[21] $\boldsymbol{u}_i$ is the instantaneous fluid velocity vector at the position of particle i, and is obtained through a trilinear interpolation of the Eulerian field. Note that relative to the model in Ref. 6, the fact that $\rho_a/\rho_l \sim 10^{-3}$ is used to neglect two relative acceleration terms in Eq. (8). The Basset history term is also neglected on the basis of a small relative acceleration. In Ref. 22 and in most DNS studies in cloud physics, the change in cloud droplet radius as a result of condensation (or evaporation) is described by[22]

$$\frac{dr_i(t)}{dt} = \frac{K}{r_i(t)}\left(S_e(\boldsymbol{X},t)\right)_i\,, \tag{10}$$

where S_e is the environmental supersaturation, which is related to q_v and T by

$$S_e = \frac{q_v}{q_{v,s}} - 1\,, \tag{11}$$

where $q_{v,s}$ is the saturation water vapor mixing ratio, which can be calculated from:[23]

$$q_{v,s} = 621.97\frac{p_{sat}}{p - p_{sat}}. \tag{12}$$

p_{sat} is the saturation water vapor pressure, which is obtained from:[24]

$$p_{sat} = 611.2 \times \exp\left(\frac{17.67(T - 273.15)}{T - 29.65}\right). \tag{13}$$

The S_e is a Eulerian quantity in Eq. (11) but interpolated to the particle position in Eq. (10). Also, K is a growth parameter that depends on temperature and pressure and is expressed as[14]

$$K = \frac{1}{\left(\frac{L_h}{R_v T} - 1\right)\frac{L_h \rho_l}{k_T T} + \frac{\rho_l R_v T}{\mu_v p_{sat}}}, \tag{14}$$

The temporal rate of change in the mass of the particle population during condensation (or evaporation) can be written as[14]

$$\frac{d(m_l(\boldsymbol{x},t))}{dt} = 4\pi\rho_l \sum_{i=1}^{n} r_i^2(t)\frac{dr_i(t)}{dt} = 4\pi\rho_l K \sum_{i=1}^{n} r_i(t)\big(S_e(\boldsymbol{X},t)\big)_i\,. \tag{15}$$

where m_l is the mass of liquid water per grid cell and n is the number of cloud droplets inside each grid cell. C_d can be determined as[14]

$$C_d(\boldsymbol{x},t) \equiv \frac{d(m_l(\boldsymbol{x},t))}{m_a dt} = \frac{4\pi\rho_l K}{\rho_a a^3}\sum_{i=1}^{n} r_i(t)\big(S_e(\boldsymbol{X},t)\big)_i\,, \tag{16}$$

where m_a is the mass of air in each grid cell that has a volume of a^3. q_c, which appears in Eq. (3), is modeled as[14]

$$q_c(\boldsymbol{x},t) = \frac{4\pi\rho_l}{3\rho_a a^3}\sum_{i=1}^{n} r_i^3(t)\,. \tag{17}$$

D. Consideration of curvature and solute effects

A few studies[3,11] in cloud microphysics have considered the effects of curvature and solute. Consistent with those, we modify Eq. (10) to obtain Eq. (23) below by including the particle equilibrium saturation ratio s containing the curvature and solute effects, consistent with the kappa-Kohler theory,[15] which is described by

$$s = \frac{r^3 - r_d^3}{r^3 - r_d^3(1-\kappa)} exp\left(\frac{2\sigma_l M_l}{RT\rho_l r}\right). \tag{18}$$

Here, r_d is the dry radius before growth, r is the wet radius, and κ is the hygroscopicity of solute (dry aerosol). Let A be a parameter defined as[15]

$$A = \frac{2\sigma_l M_l}{RT\rho_l}. \tag{19}$$

By taking the natural logarithm of both sides of Eq. (18), we get:

$$\ln(s) = \ln\left(\frac{r^3 - r_d^3}{r^3 - r_d^3(1-\kappa)}\right) + \frac{A}{r},$$

From the Taylor expansion:

$$\ln(x) \equiv (x-1) - \frac{(x-1)^2}{2} + \frac{(x-1)^3}{3} - \frac{(x-1)^4}{4} + \cdots, \qquad 0 < x < 2$$

and ignoring the higher order terms, we have the simple approximation:

$$\ln(x) \approx (x-1), \quad \text{for } 0 < x < 2$$

where x can be s or $(r^3 - r_d^3)/(r^3 - r_d^3(1-\kappa))$, and the convergence restriction on the expansion is met for the problem being analyzed in this paper. Using this approximation and simplifying, we get:

$$s = 1 + \frac{A}{r} - \frac{\kappa r_d^3}{r^3 - r_d^3(1-\kappa)}. \tag{20}$$

The particle equilibrium supersaturation S_k can then be found as:[25]

$$S_k = s - 1 = \frac{A}{r} - \frac{\kappa r_d^3}{r^3 - r_d^3(1-\kappa)}. \tag{21}$$

The first and second terms on the right-hand side (RHS) of Eq. (21) quantify the curvature and solute effects, respectively. Note that the effects of the two terms are combined in this study. A plot of S_k versus r using Eq. (21) gives the Kohler curve.[25] The critical equilibrium supersaturation (S_c) and the critical radius (r_c)[26] can be found as the stationary point of Eq. (21), using standard gradient optimization.

$$r_c = \sqrt{\frac{3\kappa r_d^3}{A}}, \qquad S_c = \frac{2}{\sqrt{\kappa}}\left(\frac{A}{3r_d}\right)^{\frac{3}{2}}. \tag{22}$$

When curvature and solute effects are considered, the rate of change of particle radius during condensation (or evaporation) can be written as:[27]

$$\frac{dr_i(t)}{dt} = \frac{G}{r_i(t)}\left(S_e(\boldsymbol{X},t) - S_k(\boldsymbol{X},t)\right)_i . \tag{23}$$

The modified growth parameter G is defined as[27]

$$G = \frac{1}{\frac{L_h\rho_l}{k_T'T}\left(\frac{L_h}{R_vT}-1\right)(1+S_k) + \frac{\rho_l R_v T}{\mu_v' p_{sat}}}, \tag{24}$$

where k_T' and μ_v' are the modified thermal conductivity and modified water vapor diffusivity in air, respectively. They are modeled as[27]

$$k_T' = \frac{k_T}{1+\frac{k_T}{\alpha_T r\rho_a c_p}\sqrt{\frac{2\pi M_a}{RT}}}, \qquad \mu_v' = \frac{\mu_v}{1+\frac{\mu_v}{\alpha_c r}\sqrt{\frac{2\pi M_l}{RT}}}. \tag{25}$$

The parameters α_T and α_c are the thermal accommodation and mass accommodation coefficients, respectively. Their values are taken as unity in this work following Ref. 3. With the foregoing, the rate of change of mass during condensation (or evaporation) can be written as:

$$\frac{d(m_l(\boldsymbol{x},t))}{dt} = 4\pi\rho_l\sum_{i=1}^{n} r_i^2(t)\frac{dr_i(t)}{dt} = 4\pi\rho_l G\sum_{i=1}^{n} r_i(t)\left(S_e(\boldsymbol{X},t) - S_k(\boldsymbol{X},t)\right)_i . \tag{26}$$

where the condensation (evaporation) rate C_d is

$$C_d(\boldsymbol{x},t) = \frac{d(m_l(\boldsymbol{x},t))}{m_a dt} = \frac{4\pi\rho_l G}{\rho_a a^3}\sum_{i=1}^{n} r_i(t)\left(S_e(\boldsymbol{X},t) - S_k(\boldsymbol{X},t)\right)_i . \tag{27}$$

The critical radius criterion (Eq. (22)) is used to determine activation or deactivation. For an aerosol particle to be activated into a cloud droplet, it needs to grow beyond its critical radius. Similarly, for a cloud droplet to be deactivated into an aerosol particle, it has to shrink below the critical radius. According to Eq. (23), particle growth is positive when $S_e > S_k$ and negative if $S_e < S_k$. So, an aerosol particle, for which $r < r_c$, will grow as long as $S_e - S_k > 0$. It will activate into a cloud droplet when r becomes larger than r_c. Similarly, a cloud droplet, for which $r > r_c$, will shrink as long as $S_e - S_k < 0$, and deactivate into an aerosol particle when r becomes smaller than r_c.

E. Effect of aerosol size distributions

To explore potential effects of initial aerosol size distributions, both monodisperse and polydisperse dry aerosol size distributions are investigated in this work. For the monodisperse r_d distributions, all the dry aerosol particles have the same size (0.1 μm). For the polydisperse distributions, we assume lognormal, which is defined as[28]

$$f(r_d) = \frac{1}{r_d \sigma \sqrt{2\pi}} \exp\left(-\frac{(ln\, r_d - \mu)^2}{2\sigma^2}\right). \quad (28)$$

where $f(r_d)$ is the normalized size distribution function, and μ and σ are the mean and standard deviation of r_d, respectively.

III. SIMULATION DETAILS

We conduct two studies: Study I and Study II. The first is for **condensation and activation of aerosol particles** into cloud droplets, while the second is **for evaporation and deactivation of cloud droplets** into aerosol particles. Note that activation and deactivation occur simultaneously in natural cloud environment, but they do so at different physical locations within the cloud. Given the small model size in the present work, it will be inordinately difficult to simulate activation and deactivation at the same time. So, we design two separate studies that correspond to activation in one physical region of a cloud and deactivation in another.

A. The numerical model

The statistics of the turbulent velocity field at 6 s are listed in Table I to show the magnitudes of the turbulence statistics that are involved in this study. These statistics include the turbulent kinetic energy (TKE), $\hbar$, its dissipation rate, ϵ, the root-mean-square velocity fluctuation, u_{rms}, the Kolmogorov length scale $\eta = (\nu^3/\epsilon)^{1/4}$, the Taylor micro-scale, $\lambda = \sqrt{10(\nu)(\hbar)/\epsilon}$, the length scale characterizing large eddies, $l_0 = (\hbar)^{3/2}/\epsilon$, the forcing Reynolds number,[29] $Re_f = (\epsilon^{1/3})(k_{min}^{-4/3})/\nu$, where $k_{min} \equiv 2\pi/L = 12.27$ is the minimum wavenumber, the Taylor-scale Reynolds number, $Re_\lambda = (u_{rms})(\lambda)/\nu$, and the Reynolds number based on l_0, $Re_{l_0} = (u_{rms})(l_0)/\nu$. Table I shows that the TKE varies between 0.00183 and $0.0165\ m^2/s^2$, with corresponding dissipation rate values of 0.00019 and 0.01172 m^2/s^3 and u_{rms} values of 0.0605 and 0.1817 m/s. The ranges for Taylor microscale λ, integral scale l_0, and their respective Reynolds numbers are (0.0252,0.0667) m, (0.181, 0.423) m, (134.200, 534.950), and (1707, 2911), respectively. The ranges for forcing Reynolds number Re_f and Kolmogorov length scale η are (134.20, 534.95) and (0.00073, 0.0020) m, respectively. These values are within the scope of the ambient microscale cloud environment.[30]

TABLE I. Statistics of the turbulent fields at 6 s

Turbulence level	$\hbar$ (m^2/s^2)	ϵ (m^2/s^3)	u_{rms} (m/s)	λ (m)	η (m)	l_0 (m)	Re_f	Re_λ	Re_{l_0}
Very high	0.0165	0.01172	0.1817	0.0252	0.00073	0.181	534.950	304.988	2910.96
High	0.00768	0.00293	0.1239	0.0343	0.00103	0.229	336.939	283.698	1890.67

Medium	0.00397	0.00072	0.0890	0.0497	0.00147	0.347	211.092	295.192	2061.35
Low	0.00183	0.00019	0.0605	0.0667	0.00200	0.423	134.200	269.107	1706.74

The physical model simulated in this work is that of a cubic domain (box) inside which turbulence, cloud, and aerosol interact. A triply periodic condition is assumed on the boundaries of the cube for the primary dependent variables. It is well known in turbulence theory that the larger the ratio of box length to the integral length scale of turbulence, the less restrictive the assumption of periodicity. With due consideration for the physical microscale problem in the atmosphere,[30] the computational domain is set to $0.512^3\ m^3$ in the present study, as in Ref. 14. The domain is divided equally into cloudy and clear-air fractions (Fig. 1) at the beginning of the simulations. The cloudy region is assumed to always be supersaturated while the clear-air region can be just saturated or subsaturated. Initially, only the former contains cloud or aerosol particles, but subsequent turbulent mixing causes the particles or droplets to spread to all parts of the domain. A slab-like cloud configuration (Fig. 1) is assumed for the initial field,[14] to enable a sharp transition (Fig. 2) in the temperature and vapor mixing ratio at the cloud/clear-air interface.

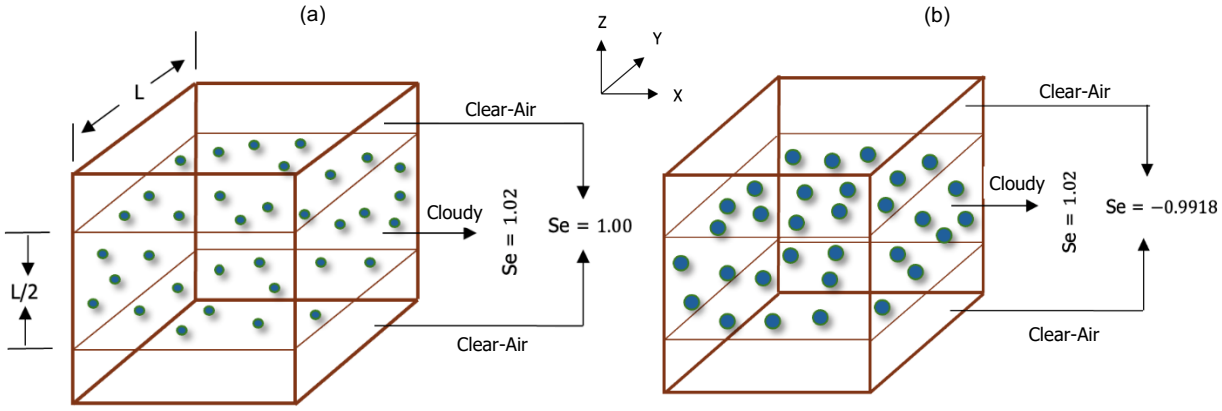

FIG. 1 Initial configurations for (a) Study I, and (b) Study II. The middle half represents the cloudy region while the top and bottom one-fourths constitute the clear-air region. The cloudy region is initially 2% supersaturated in both studies while the clear-air region is just saturated in the first and −99.18% subsaturated in the second. The spheres represent aerosol particles in Study I and cloud droplets in Study II.

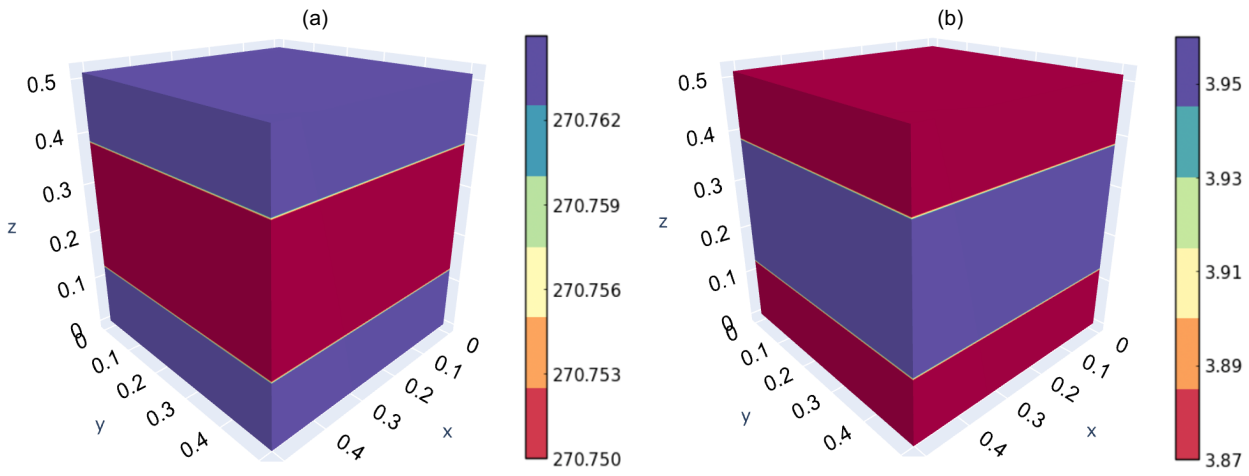

FIG. 2 Contour plots of (a) initial temperature and (b) initial vapor mixing ratio, in Study I. A sharp transition is visible in the temperature and vapor mixing ratio profiles. The initial profiles in Study II are similar but have different magnitudes.

The thermodynamic fields and particles are initialized as follows. In Study I, the cloudy region is supersaturated, while the clear-air region is just saturated. The initial vapor mixing ratio field is specified as:[14]

$$q_v(z, t=0) = \begin{cases} q_v^{max}, & d - L \times 0.5 \times 0.5 \le z < d + L \times 0.5 \times 0.5 \\ q_{v,e}, & elsewhere \end{cases}. \tag{29}$$

The value of $q_{v,s}$ in Eq. (12) is 3.872 g/kg. Above, $q_v^{max} = 1.02 \times q_{v,s} = 3.949\ g/kg$, and $q_{v,e} = 3.872\ g/kg$. The length, $d \equiv L/2$ is the width of the cloud slab. By setting $\boldsymbol{F}_b = 0$ and $q_c = 0$ (in the initial field) in Eq. (3), the temperature field is initialized as:[14]

$$T(t=0) = \langle T(t=0) \rangle - 0.608 \langle T(t=0) \rangle (q_v(z, t=0) - \langle q_v(t=0) \rangle) . \tag{30}$$

At the start of the simulations, a total of 8.8×10^6 dry aerosol particles are randomly placed in the cloudy region, giving a number concentration of 65.565 cm^{-3}. The simulations start from dry aerosol radii. We simulate six Cases: H, H-M, H-L, V-L, M-L, and L-L, which are summarized in Table II. The identifiers 'H', 'V', 'M', and 'L', when positioned before the dash (-) imply 'high', 'very high', 'medium', and 'low' turbulence intensities, respectively. The identifiers 'M' and 'L', when positioned after the dash (-) indicate 'monodisperse' (M) and 'lognormal' (L) dry aerosol size distributions. Dry aerosol radius (r_d) is 0.1 μm and the distributions are monodisperse for Cases H and H-M. For lognormal distributions (L), the geometric mean (μ) is 0.1 μm, the standard deviation (σ) is 0.015 μm, the maximum r_d is 0.22 μm and the minimum r_d is 0.04 μm. The curvature and solute effects are thoroughly neglected in Case H. Equation (10) is used to model the particle growth in Case H while Eq. (23) is used in all other cases. Using the mean value of 0.1 μm, the initial volume fraction occupied by aerosol particles is approximately equal to 2.75×10^{-11} %,

which gives a Stokes number (S_t) of 6.37×10^{-8}, for Study I. Under this condition, the particle is essentially a tracer that is freely carried around by the continuous air phase.

TABLE II. Cases in Study I and Study II. Case H has 'high' turbulence level and 'monodisperse' dry size distribution but does not model curvature and solute effects. Case H-M is Case H but with inclusion of curvature and solute effects. Cases H-L, V-L, M-L, and L-L have 'lognormal' dry size distribution and include curvature and solute effects. Their turbulence levels are 'high', 'very high', 'medium' and 'low', respectively. The initial size distribution of cloud droplets is monodisperse.

Case	Dry aerosol size (μm)	TKE dissipation rate (m^2/s^3)	Turbulence level	Curvature and solute effects	Initial particle size in Study I (μm)	Initial particle size in Study II (μm)
H	0.1	2.93×10^{-3}	High	No	0.1	15
H-M	0.1	2.93×10^{-3}	High	Yes	0.1	15
H-L	0.1 ± 0.015	2.93×10^{-3}	High	Yes	0.1 ± 0.015	15
V-L	0.1 ± 0.015	1.17×10^{-2}	Very high	Yes	0.1 ± 0.015	15
M-L	0.1 ± 0.015	7.2×10^{-4}	Medium	Yes	0.1 ± 0.015	15
L-L	0.1 ± 0.015	1.9×10^{-4}	Low	Yes	0.1 ± 0.015	15

In Study II, the cloudy region is supersaturated, but the clear-air region is subsaturated. The same configuration as in Eq. (29) is used except that $q_{v,e} = 0.03138\ g/kg$, indicating a subsaturated environment. The temperature field is also initialized like in Eq. (30). A total of 8.8×10^6 cloud droplets, each having a radius of $15\ \mu m$, are randomly placed in the cloudy region at the start. The initial volume fraction occupied by cloud droplets and Stokes number (S_t) in Study II are respectively 9.27×10^{-5} % and 1.43×10^{-3}. We again simulate six Cases (Table II) in Study II. Note that particles have a zero velocity at the initial time.

B. List of parameters

We tabulate the constants and initial values of the relevant parameters in Table III. Since our domain length is small ($0.512\ m$), the air density and ambient pressure can be taken as constants at that altitude. A hygroscopicity parameter (κ) of 0.61 is used to represent ammonium sulfate aerosols.[31]

TABLE III. List of parameters and their values

Symbol	Value	Unit	Symbol	Value	Unit
$q_{v,s}$	3.8725	g/kg	$q_{v,e}$	3.8725 (Study I) 0.03138 (Study II)	g/kg
q_v^{max}	3.949	g/kg			
L_h	2.5×10^6	J/kg	c_p	1005.0	J/kg/K
ρ_a	1.0	kg/m^3	R	8.314	J/mol/K

ρ_l	1000	kg/m^3	p	82844.14	N/m^2
$\langle T(t=0)\rangle$	270.75	K	R_d	287.0	J/kg/K
ν	1.5×10^{-5}	m^2/s	R_v	461.5	J/kg/K
k_T	0.0238	W/m/K	p_{sat}	512.617	N/m^2
μ_T	2.16×10^{-5}	m^2/s	σ_l	0.072	N/m
μ_v	2.16×10^{-5}	m^2/s	M_l	0.018	kg/mol
κ	0.61	-	M_a	0.029	kg/mol
k_{min}	12.27	1/m	S_t	6.37×10^{-8} (Study I)	-
k_{max}	1571	1/m		1.43×10^{-3} (Study II)	-

C. Numerical implementation

The FronTier computational fluid dynamics software package[32] has been used to solve the model equations used in this study. The convective terms are solved using the finite-difference based fifth order weighted essentially non-oscillatory (WENO) scheme. A projection scheme is used, and the Poisson equation is solved for the pressure field. The PETSc package[33] is adopted to solve the systems of linear equations that arise from the discretization of the diffusion terms in Eqs. (1), (5), and (6). The Crank-Nicolson scheme is used as the time integration method. The ordinary differential equations for particle propagation, Eqs. (7) and (8), are solved with the implicit Euler method. Parallelization is achieved based on domain decomposition and the message passing interface (MPI) protocol.

The $k_{max}\eta$ value for Cases H, H-M, and H-L is 1.62, where k_{max} is the maximum wavenumber and η is the Kolmogorov spatial scale. The corresponding values for Cases V-L, M-L, and L-L are 1.15, 2.30, and 3.14. Based on the recommended lower bound of 1.5 for this parameter ($k_{max}\eta$),[13] we should have good resolution of the small scales of turbulence except perhaps for Case V-L. To assess the impact of grid resolution, we compared the TKE spectra, $E(k)$[34] for simulations that use 64^3, 128^3, 256^3, and 512^3 grid points, for the domain size of $0.512^3\ m^3$. Figure 3 shows that the spectra are essentially identical for 256^3 and 512^3 for the range of wavenumbers that significantly contribute to the integral of this quantity to give the TKE. Hence, we conclude that the 256^3 mesh gives an acceptable compromise between computational cost and accuracy.

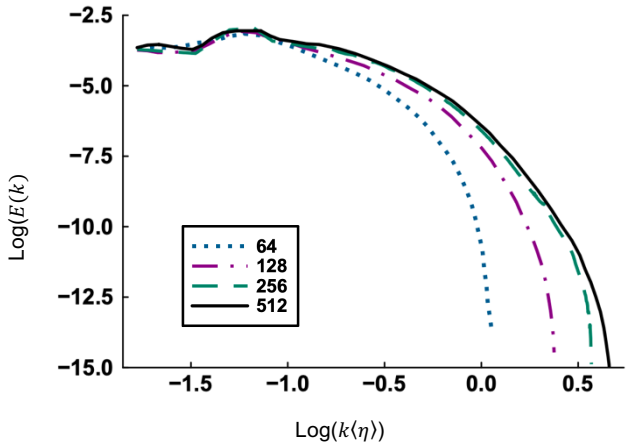

FIG. 3 The TKE spectra for four grid resolutions in logarithmic scale. The plots represent Case H-L at 3 s. Note that wavenumbers (k) in the abscissa are multiples of k_{min} and are in the radial coordinate direction. The legend labels indicate the number of grid points in one coordinate direction.

As mentioned in Gao et al.[14], one reason for developing a finite-difference based DNS model is the need to model the sharp cloud/air interface (Eq. (29)) which is found in cumulus clouds.[35] Although the pseudospectral method is generally more accurate than the finite difference method for solving the incompressible Navier-Stokes equations,[36] the discontinuity between the cloudy and clear-air regions (Fig. 2) will pose difficulties for the pseudospectral scheme and cause artificial oscillations (Gibbs phenomenon), resulting in wrong simulation results. Mittet[37] has shown that the pseudospectral scheme loses accuracy when a sharp interface is present. In a DNS study of clouds, Kumar et al.[20] introduced a smooth function in the initial water vapor mixing ratio field to avoid numerical overshoots caused by the pseudospectral method. An example of a DNS investigation of cloud physics that use the finite difference method can be found in MacMillan et al.[38] who studied the Pi chamber, for which the no-slip condition has to be imposed at the top and bottom walls, while using the pseudospectral method in the horizontal, periodic directions. The flexibility of finite difference method will allow incorporation of no-slip boundary conditions in our model in the near future. Note that use of finite difference for DNS is commonplace in the physics and mechanical engineering literature.

We utilize the high-performance computing environment offered by the Perlmutter supercomputer managed by National Energy Research Scientific Computing Center (NERSC), United States Department of Energy, USA for the simulations.

D. DNS model validation

We chose the FronTier code because of its ability to simulate two-phase flows. For example, Bo et al.[39] employed it to solve the Navier-Stokes equations and track the interface separated by two incompressible fluids having different densities. Their results matched the experimentally obtained correlations of Wu and Fateh.[40] Du et al.[41] applied the

code to calculate rotating slotted disk flows, and swirling ellipsoid and reversal flow tests. They were able to produce the correct topological bifurcations. Within the context of clouds, Gao et al.[14] developed a DNS model with Lagrangian microphysics and used an older version of the FronTier code. To validate our DNS model, we ran the updated FronTier code using the parameters of Kumar et al.[20], wherein the latter reference used a pseudospectral code. The profiles of the variance of vapor mixing ratio are plotted in Fig. 4(a). Case K-2014 in the graph represent the data from Kumar et al.[20] (Case S3). The domain size is $0.512^3\ m^3$ and the grid resolution is 512^3. Cases K-256 and K-512 are our runs, which are based on 256^3 and 512^3 grid points, respectively, but with the same parameters and initial conditions as K-2014. We run Case K-512 for only first 5 s to save computational cost, while still observing the effect of grid resolution. Excellent agreement is evident between K-2014, K-256, and K-512 in Fig. 4(a). We also run our model using the configuration of Gao et al.[14] and compare the time evolutions of mean supersaturation in Fig. 4(b). Case G-2018 represent the data from Gao et al.[14] (Case F3) while Case G-256 is our run. Complete agreement between G-2018 and G-256 is found in Fig. 4(b).

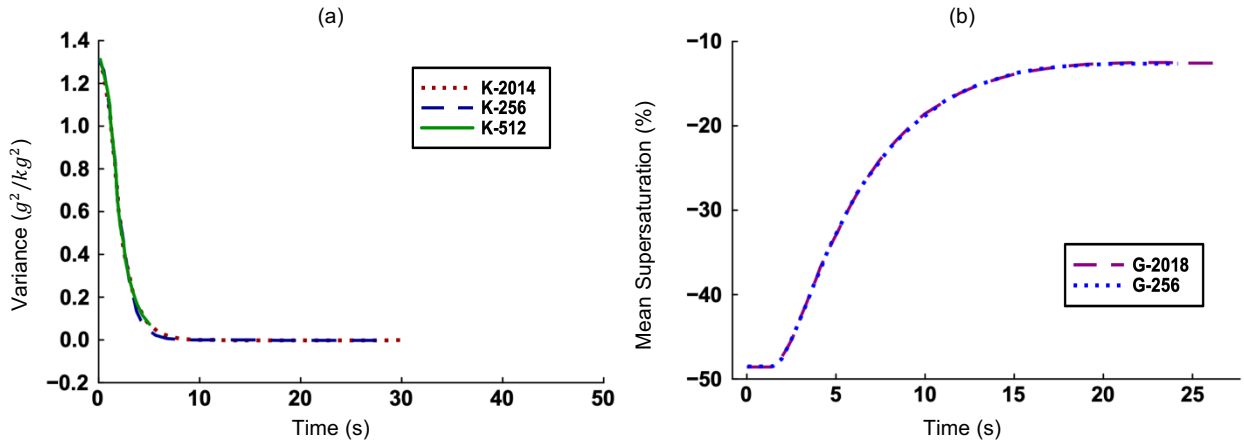

FIG. 4 Time evolution of the (a) variance of water vapor mixing ratio, and (b) mean supersaturation.

IV. RESULTS AND DISCUSSIONS

The results from our simulations are presented and discussed in this section. We first present the impact of dry aerosol size and the initial distributions on activation (Study I) and deactivation (Study II), followed by the role of turbulence intensity on activation (Study I) and deactivation (Study II). A more detailed discussion of the role of turbulence fluctuations is included in Sec. V. Some details on turbulence forcing are provided in an appendix.

A. The effects of dry aerosol size on activation and deactivation

1. Activation

Study I is primarily concerned with vapor condensation and aerosol activation. The temporal evolutions of the mean temperature, mean vapor mixing ratio, and mean environmental supersaturation, are plotted in Figs. 5(a)-(c) for Cases H, H-M, and H-L. These are the first three cases in Table II, which have the same turbulence intensity (high here) but differ in the treatment of the initial dry aerosol size distribution. We find in all the three cases that the mean temperature increases with time while the mean supersaturation and mean vapor mixing ratio decrease. Since water vapor condenses to become liquid water, particles grow bigger by absorbing the water while the vapor mixing ratio and supersaturation decrease. This is accompanied by an increase in the temperature due to latent heating. The attention of the reader is drawn to the small range of values on the ordinate of the graphs in Figs. 5(a)-(b) for the domain-averaged temperature and vapor mixing ratio. Assuming a mean value of 270.78 K, the relative variation in the temperature for Case H is approximately $(270.797 - 270.756)/270.77 \times 100\% = 0.015\%$, which is small. The corresponding value for the vapor mixing ratio is approximately 0.41%, which is also small. The change in the supersaturation over 24 s (Fig. 5(c)) is almost 108.17%, which is significant. Hence, significant variations in supersaturation are possible even when the changes in vapor mixing ratio and temperature are small. We also see that Case H, which does not consider the curvature and solute effects, shows the most rapid rise (decay) in temperature (supersaturation) of all the three cases. The results for Cases H-M and H-L are almost identical in Figs. 5(a)-(c), suggesting that the initial dry aerosol size distribution does not appear to affect the evolution of the mean quantities. The mean profiles in Figs. 5(a)-(c) follow a linear trend between 1 s to approximately 15 s. The corresponding linear regression fittings are 270.76 + 0.0018x, 3.91 – 0.00075x, and 0.00947 – 0.00033x, where x is the independent variable for a particular graph. At later times, the mean thermodynamic fields change more slowly because most of the water vapor has already been converted to liquid water in the form of cloud droplets. The results are consistent with the understanding that liquid water content and thus temperature and supersaturation are primarily determined by the dynamics and thermodynamics, with minimal influences by the initial aerosol size distributions.

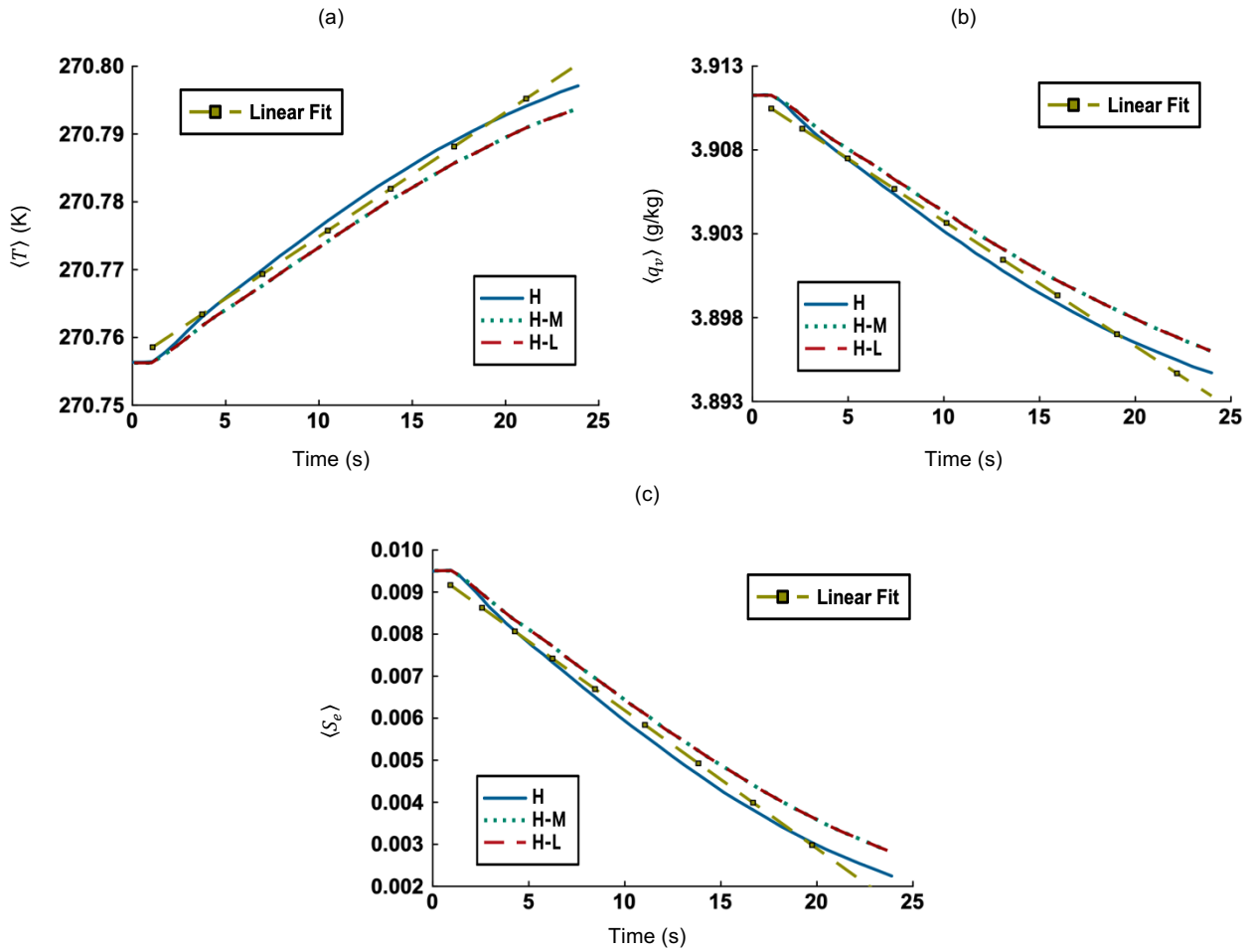

FIG. 5 Time evolution of (a) mean temperature ($\langle T \rangle$), (b) mean water vapor mixing ratio ($\langle q_v \rangle$), and (c) mean environmental supersaturation ($\langle S_e \rangle$). The linear fit is indicated by a dashed line with 'square' markers. 'H' before dash (-) stands for 'high' turbulence. 'M' and 'L' after dash (-) imply 'monodisperse' and 'lognormal' distributions.

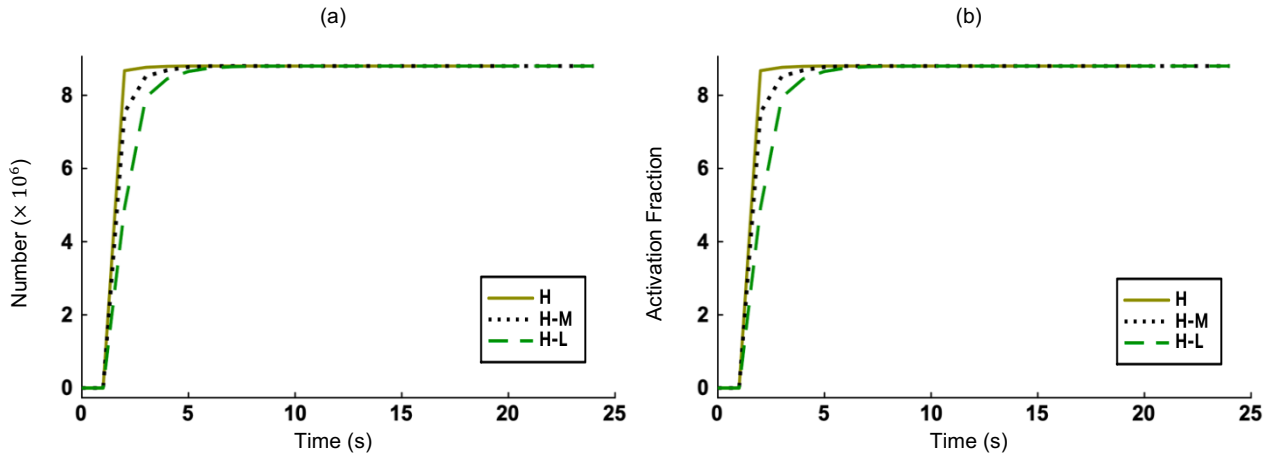

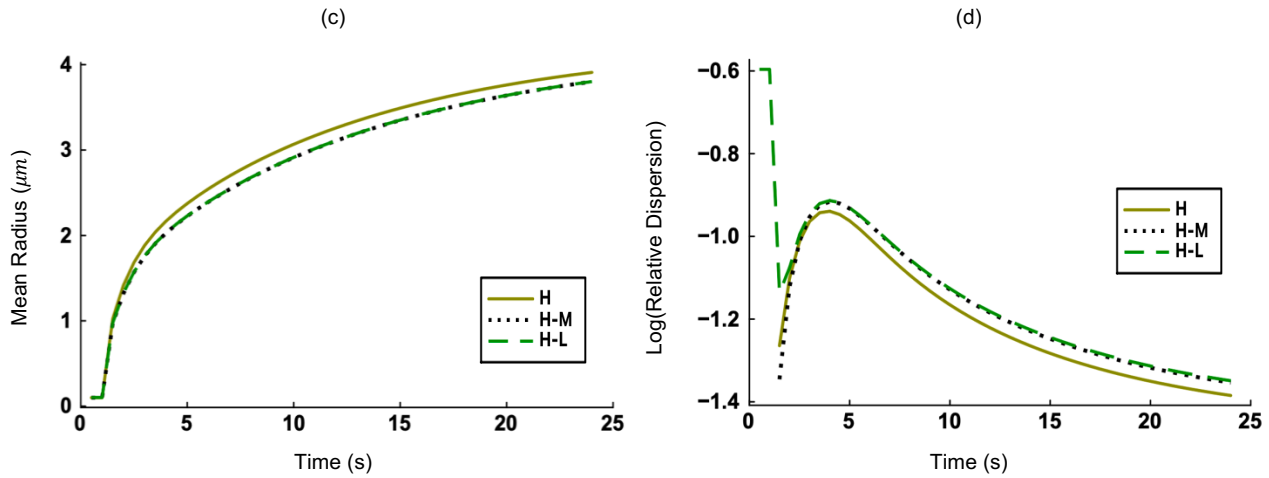

FIG. 6 Time evolution of (a) number of activated aerosol particles, (b) activation fraction, (c) mean radius of all particles, and (d) relative dispersion of particle radius in logarithmic scale in Study I. 'H' before dash (-) stands for 'high' turbulence. 'M' and 'L' after dash (-) imply 'monodisperse' and 'lognormal' distributions.

The temporal evolution of activated aerosol particle number for the same three cases are shown in Fig. 6(a). Since Case H does not include curvature and solute effects, Eq. (22) cannot be applied to calculate the critical radius for activation. Rather we set the critical radius to be 1 μm, which is based on the empirical observation that cloud droplets are often considered to be larger than 1 μm.[42] We see in Fig. 6(a) that all aerosol particles activate into cloud droplets in approximately 4 s, 5 s, and 6 s for Cases H, H-M, and H-L, respectively. The activation fraction is the ratio of activated aerosol number and total (activated + unactivated) particle number, and its time evolution is plotted in Fig. 6(b). The plot shows that activation occurs over a period of time rather than instantaneously[11] for monodisperse distributions (Case H-M). The activation profile is steeper for Case H, which has the same monodisperse distributions as H-M but no curvature and solute effects. The activation rate is slowest for Case H-L on account of the lognormal distribution.[43] Since critical radius is directly proportional to the dry radius (Eq. (22)), larger dry aerosol particles need more time to grow beyond their critical radii and activate. Figure 6(c) shows the time evolution of the mean particle radius. We point out that 'particle' is used here in a general sense and can apply to aerosol particle ($r < r_c$) or cloud droplet ($r > r_c$). It is evident that mean radius is larger for Cases H compared to Cases H-M and H-L. That is, the particle growth rate is slower and condensation is weaker when curvature and solute effects are included (Cases H-M and H-L). The relative dispersion, defined as the ratio of standard deviation to mean, of the particle radius is plotted in Fig. 6(d). The profiles for Cases H-M and H-L converge as particle radius increases, indicating that dry aerosol size distributions (monodisperse or lognormal) are less important when particles are bigger. As particles are smaller at early times, the relative dispersion of radius is higher for Case H-L due to the lognormal distribution.

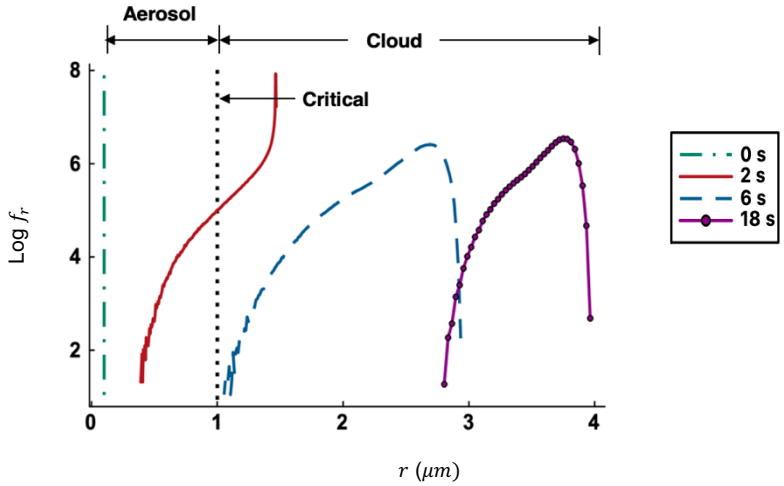

FIG. 7 Log PDFs of particle radius for Case H in Study I at selected times. The dotted line shows the critical radius (r_c).

The probability density functions of the particle radius (f_r) at 0 s, 2 s, 6 s, and 18 s for Case H are plotted in Fig. 7 in a log format. We see that f_r begins to broaden with time, with a tendency for convergence to a uniform, large radius at 18 s, relative to 6 s, where a wider variation in particle radii is evident as the particles grow from a uniform small (initial) radius to the larger radii at 18 s. The broadening at early times is a result of fluctuations in environmental supersaturation.[9] Figures 8(a)-(c) show the PDFs of radius at 2 s, 6 s, and 18 s for Case H-M, which is Case H with curvature and solute effects included. Aerosol is shown in solid lines in the figure while cloud is in dash-dot lines. Being generally of smaller size, aerosol particles are found at the lower values of the abscissa whereas cloud droplets are at the higher values. Note the differences in the radius coordinate in Figs. 8(a)-(c). Both aerosol particles and cloud droplets are present at 2 s and 6 s but only cloud droplets can be found at 18 s. All aerosol particles activate into cloud droplets over time, and the latter continue to grow as long as the local supersaturation remains positive. The PDFs of aerosol particle radii become narrower with time and aerosols no longer exist at 18 s (Fig. 8(c)).

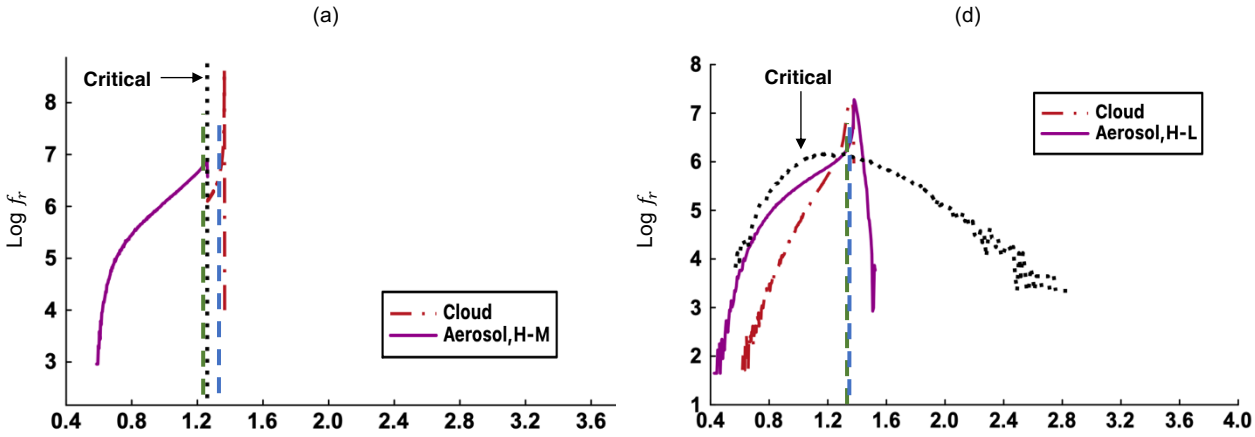

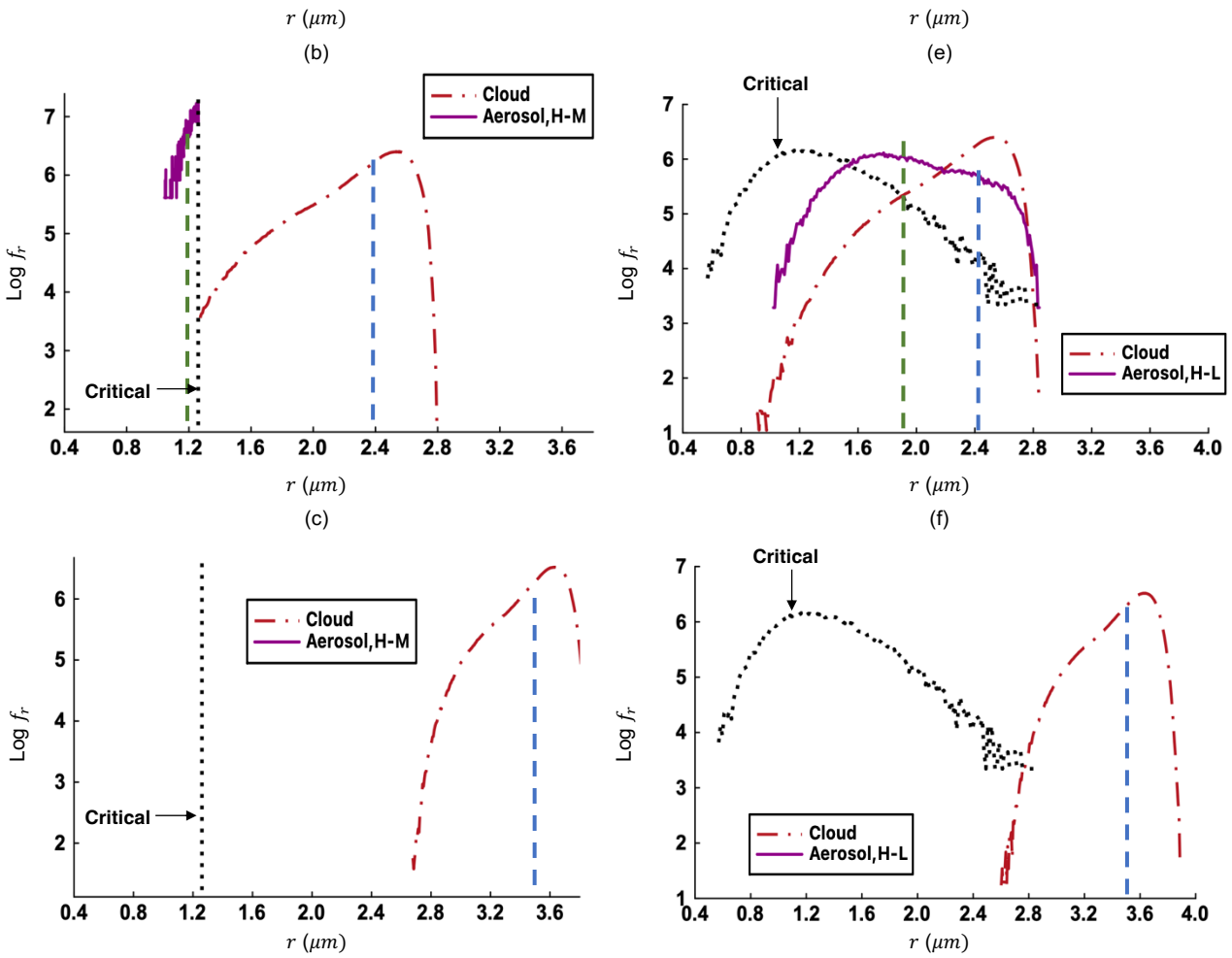

FIG. 8 Log PDFs of particle size at (a) 2 s, (b) 6 s, and (c) 18 s for Case H-M. The subplots (d), (e), and (f) are analogous for Case H-L. 'H' before dash (-) stands for 'high' turbulence. 'M' and 'L' after dash (-) imply 'monodisperse' and 'lognormal' distributions. The dotted line shows the critical radius (r_c). The green and blue dash lines show the mean aerosol and cloud droplet radii, respectively.

Figures 8(d)-(f) show the corresponding results for Case H-L. At 2 s and 6 s, there is an overlap between the PDFs of aerosol and cloud radii, with the observation that the aerosol particles are sometimes larger than the cloud droplets. The distributions at 2 s and 6 s should be contrasted with those for the Case H-M where the aerosol particles and cloud droplets do not overlap. Due to the dry aerosol particles being lognormally distributed in Case H-L, **there exists a distribution of critical radius instead of a single value**. Thus, it is possible that a smaller aerosol particle has grown beyond its critical radius and is classified as a cloud droplet while a larger aerosol particle may not yet be large enough to cross its critical barrier and so still remains an aerosol particle. We also see that aerosols eventually vanish and only cloud droplets remain at 18 s. The PDFs of radius in Figs. 8(d)-(f) remain skewed to the left meaning that most cloud droplets are larger than the mean radius.

2. Deactivation

Evaporation and deactivation are investigated in Study II. The temporal evolutions of the mean temperature, vapor mixing ratio, and environmental supersaturation in Figs. 9(a)-(c) show that, after an initial latent period, the mean temperature decreases while the mean vapor mixing ratio and the mean supersaturation increase for all the cases (H, H-M, and H-L). The temporal change is exponential until approximately 15 s, when we see a leveling-off to asymptotic values. The reduction in the mean air temperature and the increase of the mean supersaturation stem from evaporative cooling. The polynomial fits for the graphs in Figs. 8(a)-(c) are $271.53 - 0.42x + 0.021x^2 - 0.00032x^3$, $1.80 + 0.17x - 0.008x^2 + 0.00013x^3$, and $-0.56 + 0.06x - 0.0026x^2 + 0.00003x^3$, respectively. Thus, these profiles are roughly cubic, although dominated by the linear and quadratic terms. It is important to note that for the same turbulence level, neither curvature and solute effects nor dry aerosol size distribution has any significant impact on the temporal evolution of the mean quantities. This is because, despite being negative, the magnitude of mean S_e is much larger than the value of the mean S_k ($\sim$0.00061) in Study II.

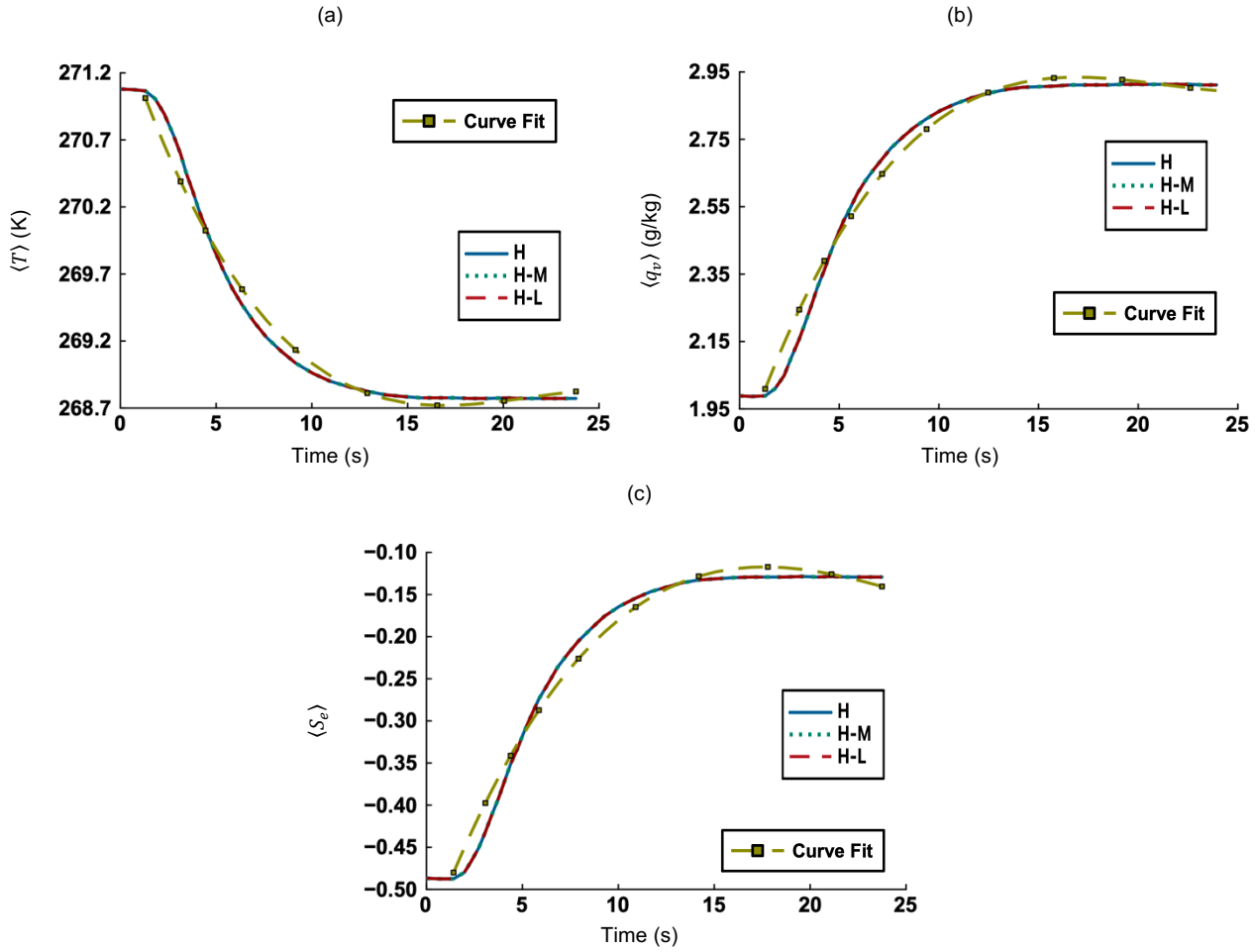

FIG. 9 Time evolution of (a) mean temperature ($\langle T \rangle$), (b) mean water vapor mixing ratio ($\langle q_v \rangle$), and (c) mean environmental supersaturation ($\langle S_e \rangle$). The curve fit is indicated by a dashed line with 'square' markers. 'H' before dash (-) stands for 'high' turbulence. 'M' and 'L' after dash (-) imply 'monodisperse' and 'lognormal' distributions.

Figure 10(a) shows the evolution of the number of deactivated cloud droplets for Cases H, H-M, and H-L. We see that the values are identical at all times for the three cases, suggesting that the initial dry aerosol size distributions do not influence the deactivation profile. Note that while we allow the initial dry aerosol size distributions to be monodisperse or lognormal in both Study I and Study II, the initial cloud droplet size distributions are monodisperse in Study II. The evolution of the mean radius in Fig. 10(b) shows that this quantity decreases with time for all three cases as a consequence of droplet evaporation. However, while the mean radius is indistinguishable at all times for Cases H-M and H-L, its decay becomes significantly slower after approximately 7 s for Case H, which is the case without curvature and solute effects. This suggests that as droplet radius r decreases and approaches r_c and r_d, curvature and solute effects begin to have an effect.

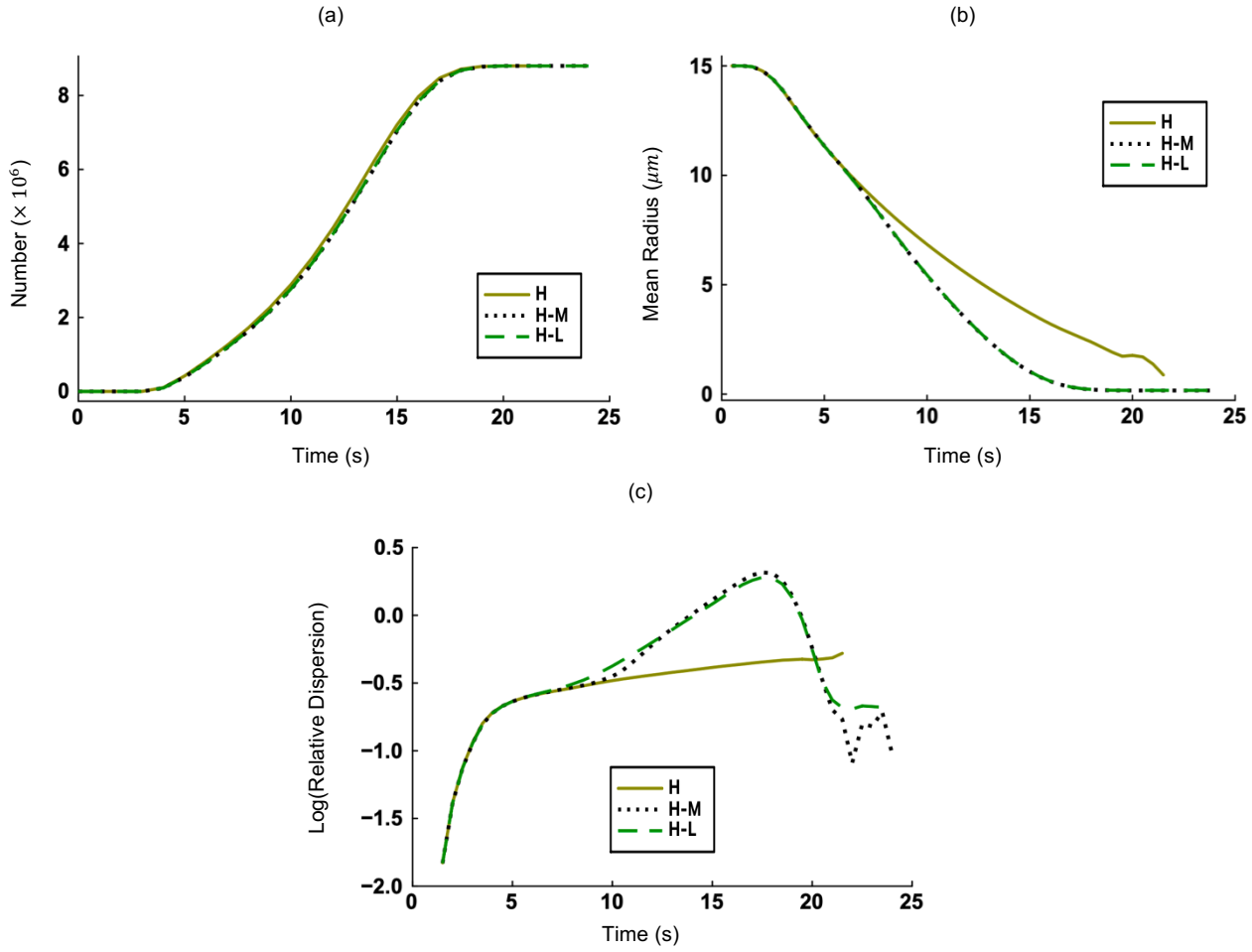

FIG. 10 Time evolution of (a) number of deactivated cloud droplets, (b) mean radius of all particles, and (c) relative dispersion of particle radius in logarithmic scale in Study II. 'H' before dash (-) stands for 'high' turbulence. 'M' and 'L' after dash (-) imply 'monodisperse' and 'lognormal' distributions.

The relative dispersion plots in Fig. 10(c) show different profiles for Case H compared to those for the other two cases after 7 s. This confirms the importance of curvature and solute effects as the radius becomes smaller. The profiles for Cases H-M and H-L are similar until 21 s. Since the r_d follows a lognormal distribution in Case H-L, the relative dispersion for this case is higher when r approaches r_d (after 21 s), consistent with Fig. 6(c). The normalized droplet size distributions for Case H (high turbulence but no curvature and solute effects) are shown in Fig. 11 at 0 s, 4 s, 10 s, and 18 s. The cloud droplets shrink significantly with time from an initial monodisperse radius of 15 μm to values in $0 < r \leq 6.5\ \mu m$ at 18 s. The PDF of radius broadens at early times, traversing the entire $0 < r \leq 15\ \mu m$ range at 4 s, but subsequently becoming narrower with time as more evaporation of cloud droplets takes place. We also see that while larger radii are more probable at early times, smaller radii particles dominate at 18 s, with a mean radius of approximately 3 μm.

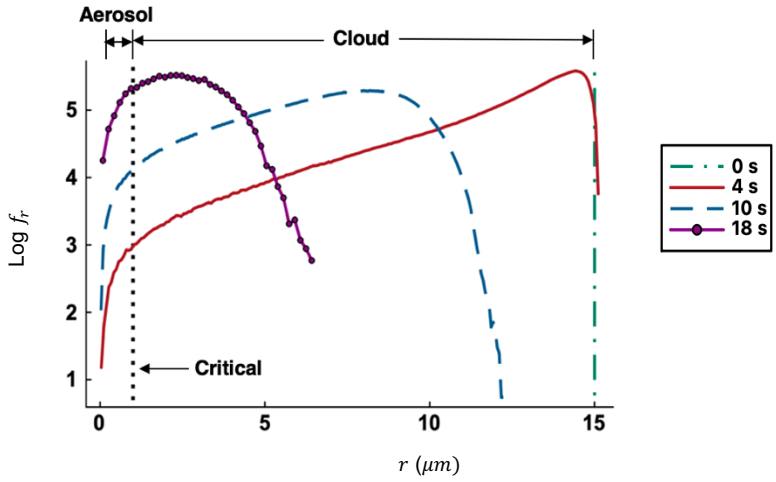

FIG. 11 Log PDFs of particle radius for Case H in Study II at selected times. The dotted line shows the critical radius (r_c).

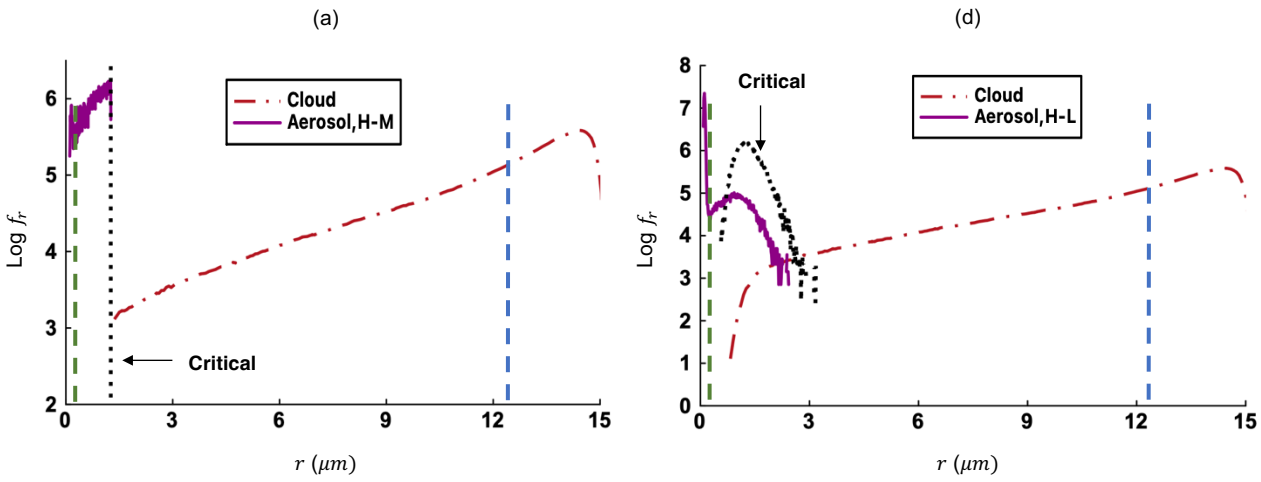

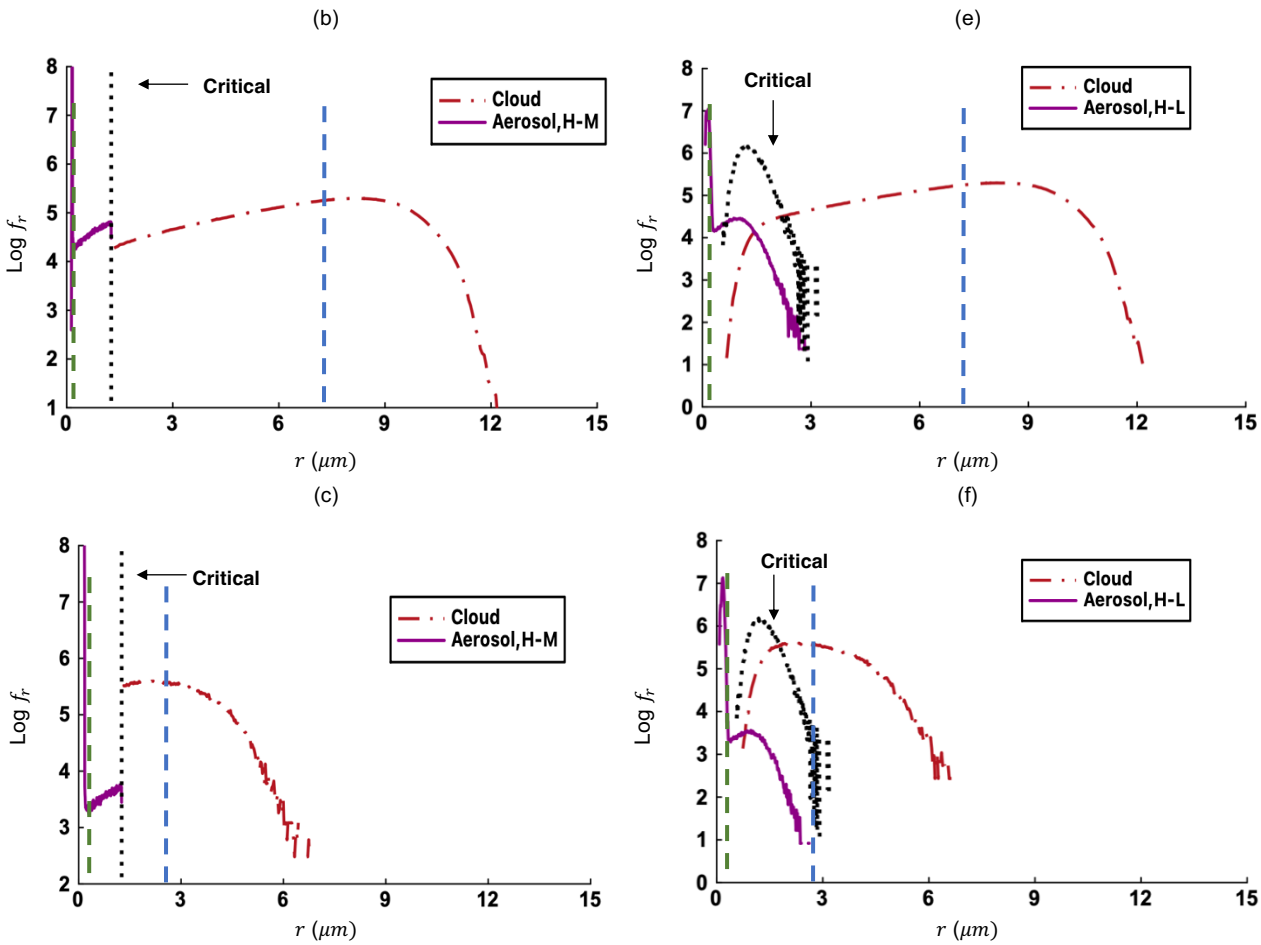

FIG. 12 Log PDFs of particle size at (a) 4 s, (b) 10 s, and (c) 18 s for Case H-M. The subplots (d), (e), and (f) are analogous for Case H-L. 'H' before dash (-) stands for 'high' turbulence. 'M' and 'L' after dash (-) imply 'monodisperse' and 'lognormal' distributions. The dotted line shows the critical radius (r_c). The green and blue dash lines show the mean aerosol and cloud droplet radii, respectively.

The PDFs of particle radius for Case H-M at 4 s, 10 s, and 18 s are plotted in Figs. 12(a)-(c). We notice that aerosol particles and cloud droplets are clearly discernible as the critical radius is single-valued due to a monodisperse dry aerosol size distribution. The corresponding results for Case H-L in Figs. 12(d)-(f) show that the f_r of aerosol particles are bimodal at the three times. That is, smaller aerosol particles ($0 < r \leq 0.5\ \mu m$) form a distribution while the larger ones ($0.5 < r \leq 3\ \mu m$) have another. The f_r of cloud droplets become narrower between 4 s to 18 s for Cases H-M and H-L. They are skewed to the left at 4 s but becomes slightly skewed to the right at 18 s for both cases, as smaller radii cloud droplets become more probable at long time, contrasted with the converse at short time.

B. The effects of turbulence intensity on activation and deactivation

The results discussed so far have been based on only one level of turbulence: H (high turbulence intensity). In this section we examine the effects of turbulence levels on the activation of aerosol particles and deactivation of cloud droplets.

1. Activation (Study I)

The time evolution of the mean environmental supersaturation and its standard deviation is plotted in Figs. 13(a)-(b) for the four turbulence levels in Study I. The plots in Fig. 13 show the time evolution after statistical stationarity has been reached. We denote this time by τ in seconds. The transient time periods required to reach $\tau = 0$ are $t = 3$ s for Case V-L, $t = 5$ s for Case H-L, and $t = 6$ s for Cases M-L and L-L, where t is the physical simulation time. The variance of environmental supersaturation $\sigma_{S_e}^2$ is defined as

$$\sigma_{S_e}^2 = \frac{\sum_i (S_{e_i} - \langle S_e \rangle)^2}{N}. \tag{31}$$

where S_e is the instantaneous environmental supersaturation, $\langle S_e \rangle$ is the mean value, and N is the number of grid points. We see that the $\langle S_e \rangle$ values are different when the respective statistically stationary states are reached (τ = 0 s in Fig. 13(a)) for the four turbulence levels, although they were the same at the beginning of simulation ($t = 0$ s). These differences are not caused by the early transients alone. The thermodynamic fields in Eqs. (5) and (6) are coupled with the dynamics of particles via the latent heat term C_d which accounts for particle size (Eq. (16)). Hence, the graphs in Fig. 13(a) demonstrate the combined effects of flow turbulence and particle size on the $\langle S_e \rangle$. We see that for the same dry aerosol size distribution (lognormal), the $\langle S_e \rangle$ is smaller for Cases L-L and M-L compared to Cases H-L and V-L. Also, $\sigma_{S_e}^2$ decays faster for Case V-L compared to the other cases during the statistically stationary periods (Fig. 13(b)). The results suggest that a higher level of turbulence leads to increased homogenization of the thermodynamic fields and a reduction in their fluctuations. Figure 13(c) shows that the relative standard deviation ($\sigma_{S_e}/\langle S_e \rangle$) decreases more, or the S_e values become less spread out compared to the mean, when the turbulence levels are higher (H-L and V-L). Hence, mixing between the cloud droplets and environmental air is more homogeneous with increased turbulence.

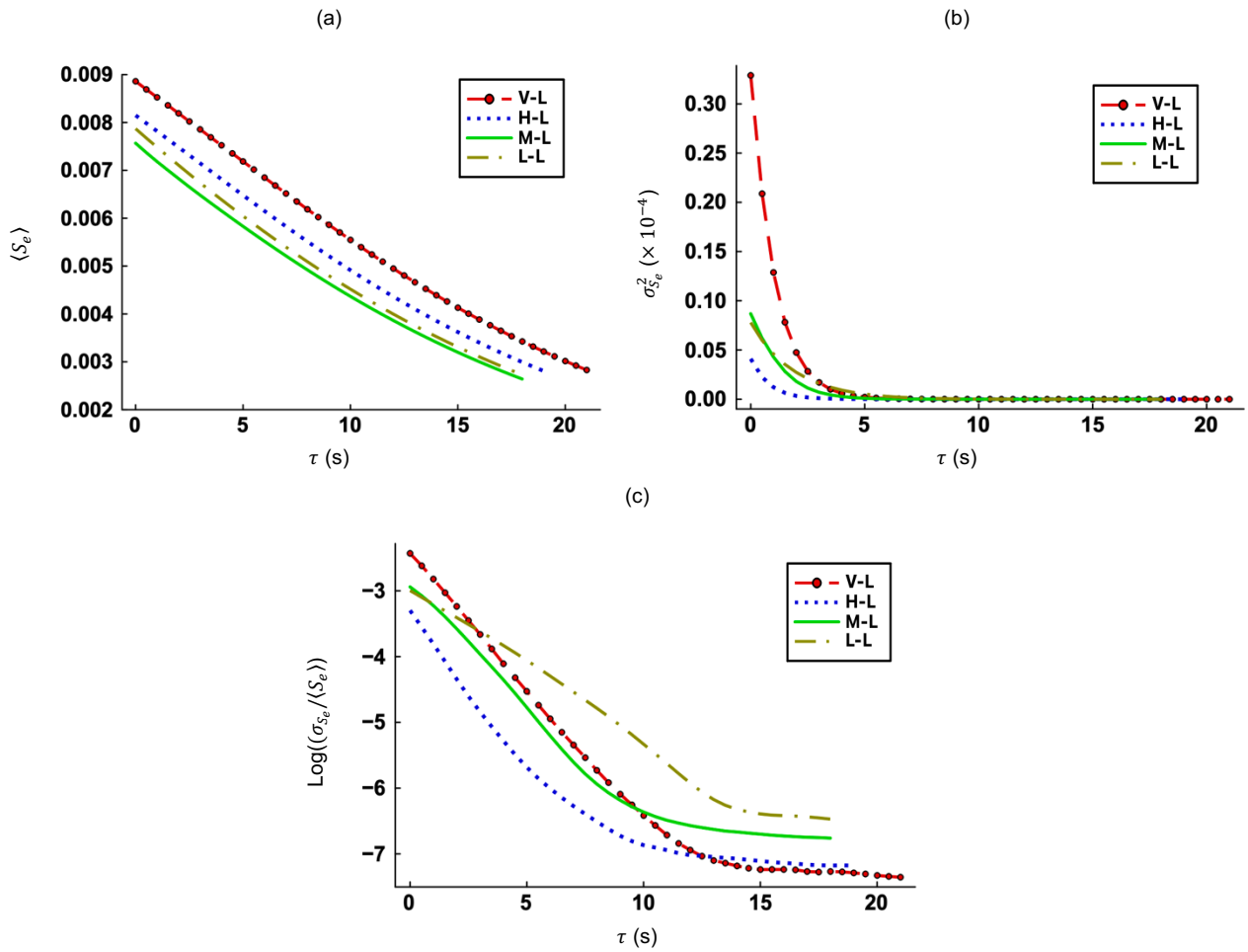

FIG. 13 Time evolution of (a) mean environmental supersaturation, (b) variance of environmental supersaturation, and (c) relative standard deviation of environmental supersaturation in a logarithmic scale in Study I. 'V', 'H', 'M', and 'L' before dash (-) stand for 'very high', 'high', 'medium', and 'low' turbulence levels.

The PDFs of S_e and S_k along with respective mean values are plotted in Figs. 14(a)-(d). We simulate two more cases with lognormal dry size distributions, namely Case H-L′ (μ = 0.33 μm and σ = 0.0026 μm) and Case H-L″ (μ = 0.22 μm and σ = 0.0089 μm) in addition to Case H-L (μ = 0.1 μm and σ = 0.015 μm). It is evident that the $\langle S_e \rangle$ is larger than the $\langle S_k \rangle$ for Cases H-L, H-L′, and H-L″ at 3.5 s (Figs. 14(a)-(c)). Therefore, particle growth is positive ($S_e > S_k$) and aerosol particles will potentially activate. For Cases H-L and H-L″, the PDFs of S_e and S_k overlap but not for Case H-L′. Thus, activation is mean-dominated[12] for Case H-L′ at 3.5 s while fluctuation-influenced activation or deactivation[12] is possible for Cases H-L and H-L″. As simulations progress, fluctuations in the S_e decrease due to mixing and there is no overlap of the PDFs at 6 s for Case H-L (Fig. 14(d)). The same is true for Cases H-L′ and H-L″. So, activation is mean-dominated for all cases at 6 s.

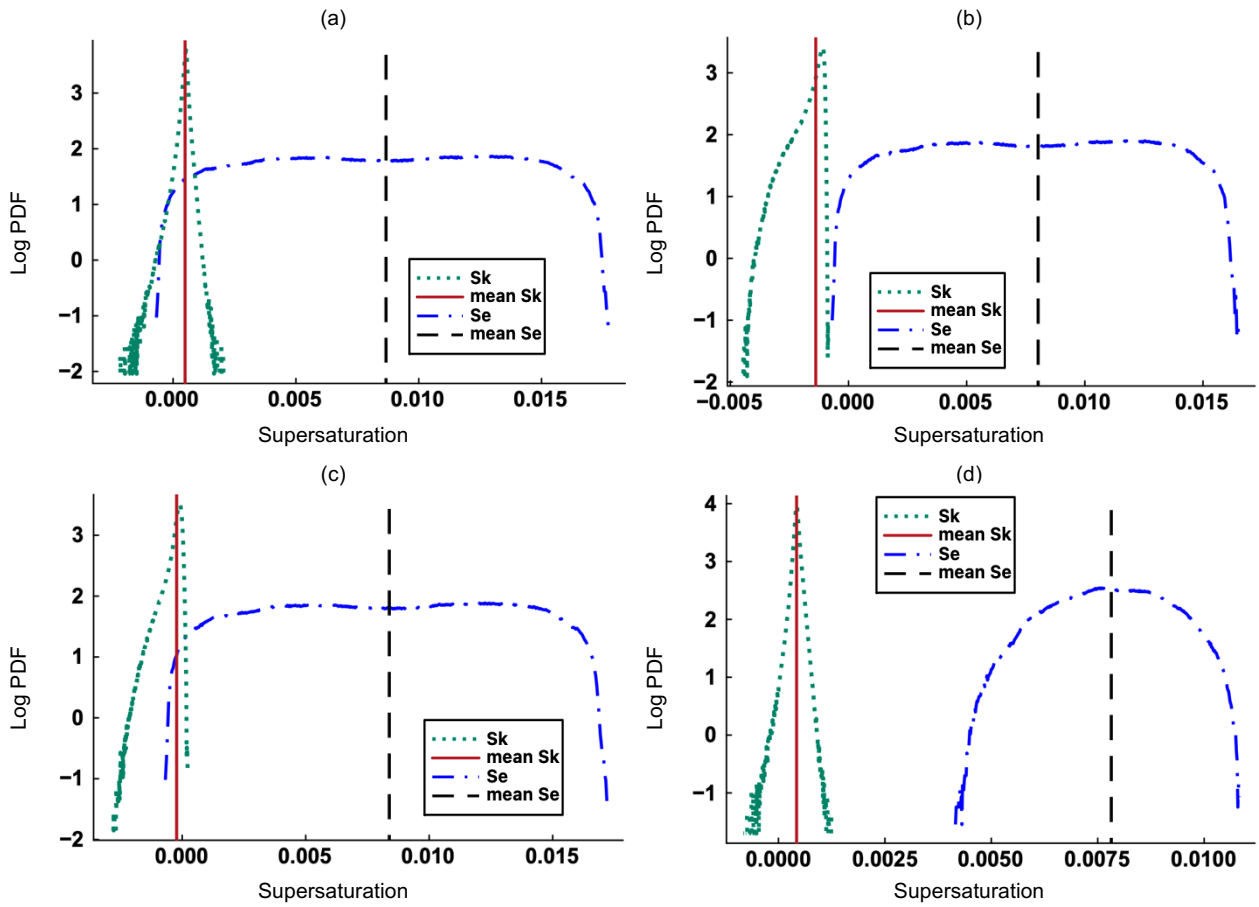

FIG. 14 Log PDFs of instantaneous supersaturation for Cases (a) H-L, (b) H-L′, and (c) H-L″, at 3.5 s in Study I. The subplot (d) is analogous for Case H-L at 6 s. The vertical lines indicate the mean values of the respective PDFs.

Figure 15(a) shows the evolution of the number of aerosol particles that activate into cloud droplets in Study I for the four turbulence cases. We see that this quantity is slightly lower for Case V-L (very high turbulence, lognormal distribution) between 2 s to 5 s compared to the other cases. Based on this observation, turbulence appears to delay activation in our model. We also report in Fig. 15(b) that the mean radius of cloud droplets is smallest for Case V-L throughout the simulation time. Note that Fig. 15(b) does not include aerosol particles. The PDFs of radius in Figs. 16(a)-(d) show that the ranges of cloud droplet radii are smallest for Case V-L. To establish some consistency with the data in Fig. 15(b), we calculate the expectation of the radius directly from the PDFs in Figs. 16(a)-(d) based on the following definition:

$$\langle r \rangle = \int_{\lambda=-\infty}^{\infty} r(\lambda) P(\lambda) d\lambda \,. \tag{32}$$

where $\langle r \rangle$ is the mean (expected) radius, r is the radius, and $P(\lambda)$ is the PDF at λ, which is an integration variable. This integral gives the mean cloud radius in the PDFs in Figs. 16(a)-(d) as: 2.581 μm, 2.685 μm, 2.809 μm, and 2.755

μm, respectively. The corresponding mean radii at 8 s in Fig. 15(b) are 2.577 μm, 2.681 μm, 2.803 μm, and 2.748 μm, respectively, which are in excellent agreement with those obtained from the PDFs. By comparing the mean droplet radii for Cases V-L and L-L, we see that the higher the turbulence intensity the slower the droplet growth rate.

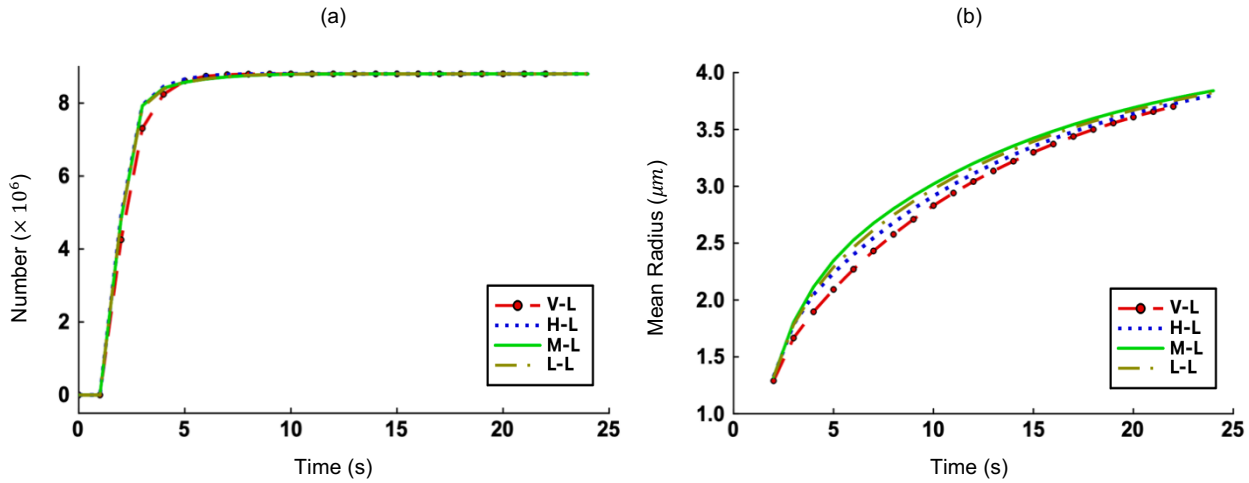

FIG. 15 Time evolution of (a) number of cloud droplets, and (b) their mean radius. 'V', 'H', 'M', and 'L' before dash (-) stand for 'very high', 'high', 'medium', and 'low' turbulence levels.

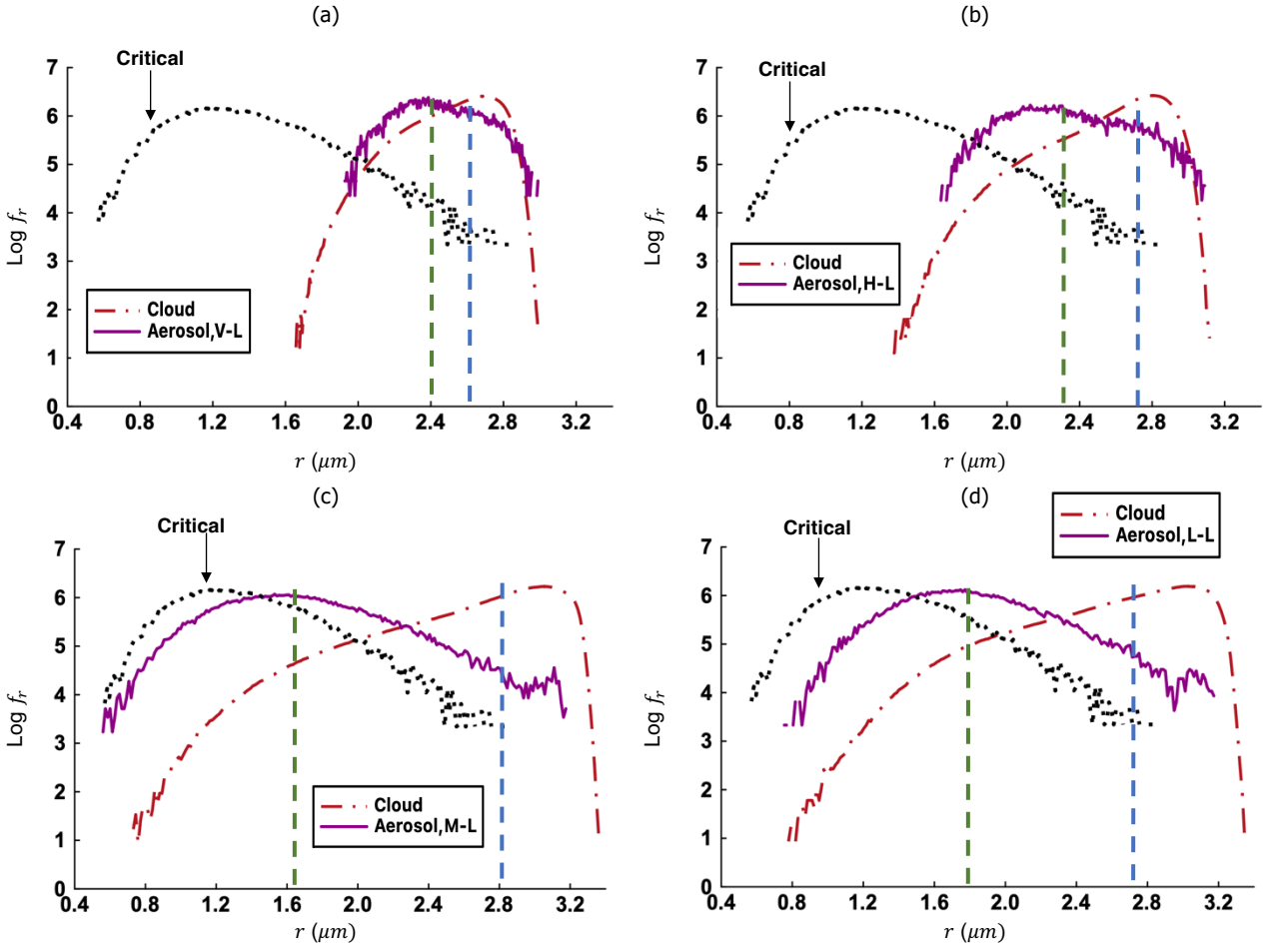

FIG. 16 Log PDF of particle size for Cases (a) V-L, (b) H-L, (c) M-L, and (d) L-L, in Study I at 8 s. 'V', 'H', 'M', and 'L' before dash (-) stand for 'very high', 'high', 'medium', and 'low' turbulence levels. The dotted line shows the critical radius (r_c). The green and blue dash lines show the mean aerosol and cloud droplet radii, respectively.

2. *Deactivation (Study II)*

Figures 17(a)-(b), which are for deactivation, correspond to Figs. 13(a)-(b) which pertain to activation. We see that the mean environmental supersaturation ($\langle S_e \rangle$) increases almost cubically with time (Fig. 17(a)), in contrast to the linear decay during activation (Study I). Also, the $\langle S_e \rangle$ increases faster for Case V-L compared to the other cases. As discussed earlier, a faster decay of $\sigma_{S_e}^2$ (Fig. 17(b)) is associated with the highest turbulence level (V-L). The relative standard deviation of S_e (Fig. 17(c)) decreases the least for Case L-L and the most for Case H-L. More cloud droplets experience partial evaporation with stronger turbulence. The opposite situation, complete evaporation of some of the droplets, is more likely when turbulence is weaker. Figures 18(a)-(b) show the PDFs of S_e and S_k for Case H-L at 5 s and 10 s, respectively. We see that $\langle S_e \rangle$ is much smaller than $\langle S_k \rangle$ and thus cloud droplets will shrink and potentially deactivate in a subsaturated environment. The PDFs of S_k are skewed to the left but most S_k values are larger than any S_e value. Hence, deactivation is mean-dominated[12] for a majority of particles. Also, the possibility of fluctuation-influenced activation or deactivation exists for some particles when the PDFs of S_e and S_k overlap.

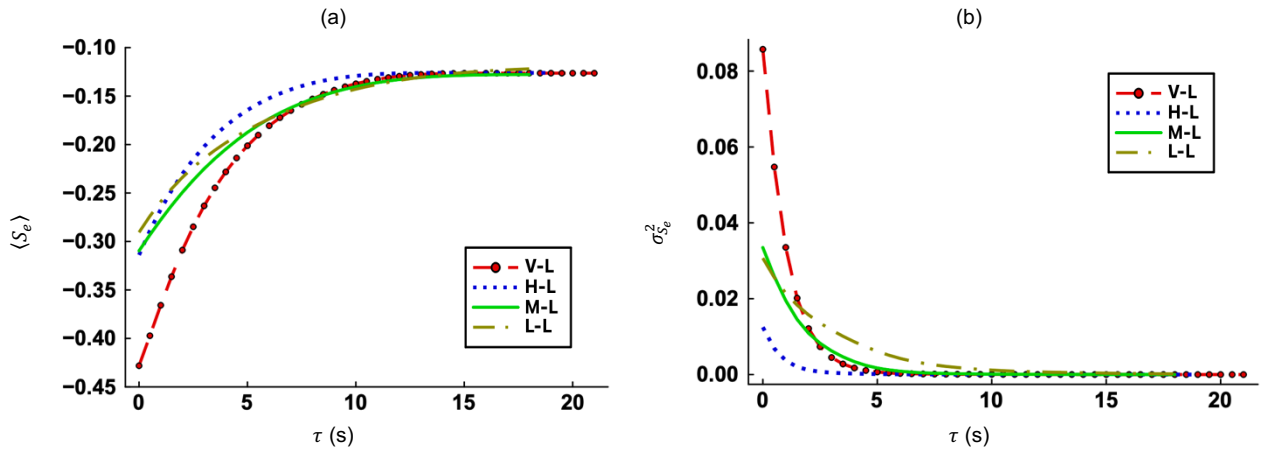

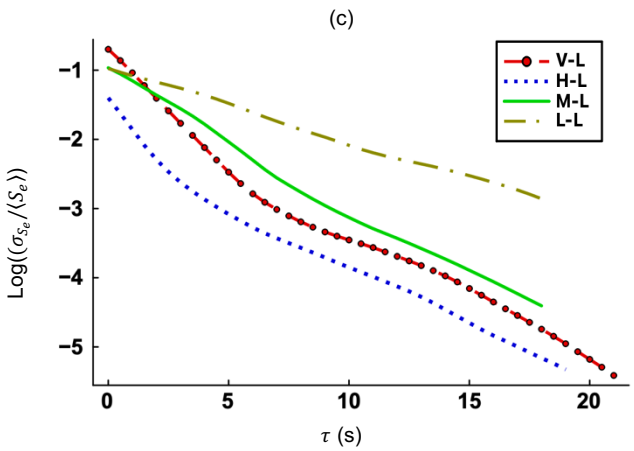

FIG. 17 Time evolution of (a) mean environmental supersaturation, (b) variance of environmental supersaturation, and (c) relative standard deviation of environmental supersaturation in a logarithmic scale in Study II. 'V', 'H', 'M', and 'L' before dash (-) stand for 'very high', 'high', 'medium', and 'low' turbulence levels.

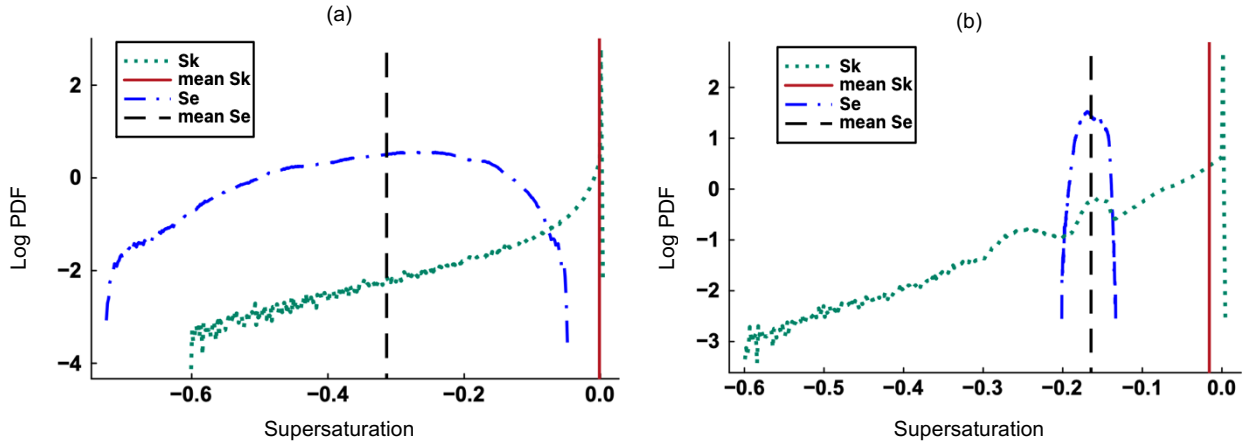

FIG. 18 Log PDFs of supersaturation for Case H-L in Study II at (a) 5 s and (b) 10 s. The vertical lines indicate the mean values of the respective PDFs.

Figure 19(a) shows the evolution of the number of cloud droplets that shrink and deactivate into aerosol particles, while Fig. 19(b) depicts the evolution of the mean radii of deactivated cloud droplets (now aerosol particles). Based on these figures, the deactivation rate is higher and mean aerosol radius is larger with higher turbulence intensity. A more efficient homogenization resulting from a higher level of turbulence causes more droplets to evaporate and allows them to shrink below their critical radii. Thus, deactivation is more rapid when the turbulence intensity is high. But we see in Fig. 19(a) that droplet deactivation rate is marginally slower for Cases V-L and H-L compared to Cases M-L and L-L before approximately 8 s. Since the deactivation process starts at roughly 4 s, we attribute the behavior between 4 s to 8 s to early transients. The slopes of the deactivation profiles are comparable for Cases V-L and H-L and also for Cases M-L and L-L. We also see that deactivation occurs between 4 s to 17 s (Fig. 19(a)) while activation happens between 1 s to 6 s (Fig. 15(a)) for Case H-L. The activation period is shorter than the deactivation period for

the same turbulence level and same critical radii. Since initial particle size is larger in Study II compared to Study I (Table II), more time is required to reach the critical radii during evaporation (deactivation).

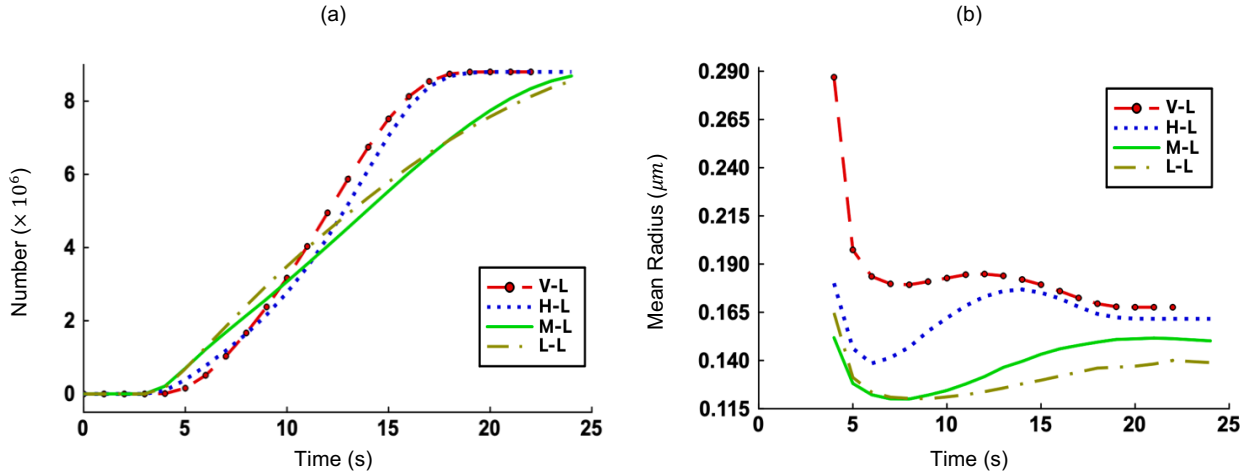

FIG. 19 Evolution of (a) number of aerosol particles, and (b) their mean radius. 'V', 'H', 'M', and 'L' before dash (-) stand for 'very high', 'high', 'medium', and 'low' turbulence levels.

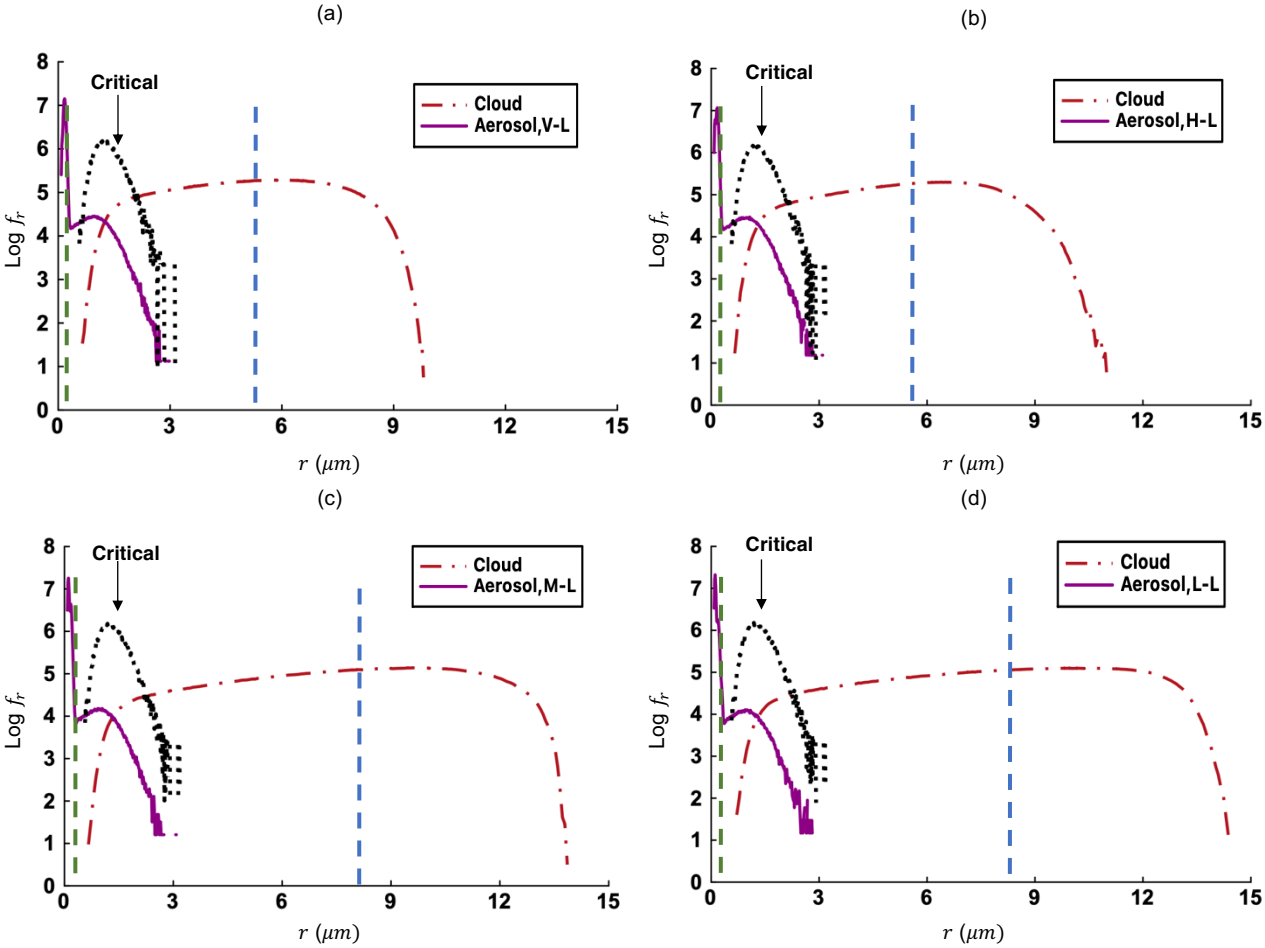

FIG. 20 Log PDF of particle size for Cases (a) V-L, (b) H-L, (c) M-L, and (d) L-L, in Study II at 12 s. 'V', 'H', 'M', and 'L' before dash (-) stand for 'very high', 'high', 'medium', and 'low' turbulence levels. The dotted line shows the critical radius (r_c). The green and blue dash lines show the mean aerosol and cloud droplet radii, respectively.

According to Fig. 19(b), the mean radii of aerosol particles do not decrease monotonically. Theoretically, they should converge to their mean dry radii (0.1 μm for all four cases). Figures 20(a)-(d) show the PDFs of radius at 12 s. The maximum cloud droplet radius is largest (14.33 μm) (Fig. 20(d)) for Case L-L (low turbulence, lognormal) and smallest (9.78 μm) (Fig. 20(a)) for Case V-L (very high turbulence, lognormal). The maximum cloud droplet radii for Cases H-L and M-L are 10.97 μm and 13.82 μm, respectively. We calculate the mean radii of aerosol particles in Figs. 20(a)-(d) using the PDFs. The values are respectively: 0.192 μm, 0.180 μm, 0.137 μm, and 0.129 μm. The corresponding values at 12 s from Fig. 19(b) are 0.185 μm, 0.173 μm, 0.132 μm, and 0.124 μm. Agreement is evident. Therefore, we confidently say that mean aerosol radius is larger at 12 s if the level of turbulence is higher. Interestingly, the mean cloud droplet radii in Figs. 20(a)-(d) are 5.29 μm, 5.57 μm, 8.07 μm, and 8.34 μm, respectively. This suggests that a stronger turbulence intensity leads to more evaporation and smaller cloud droplets. Turbulence causes cloud droplets with radii just above the critical radii (r_c) to shrink to just below the r_c and be classified as aerosol particles. This leads to a larger mean radius for aerosol particles (Fig. 19(b)).

V. FURTHER DISCUSSIONS ON TURBULENT FLUCTUATIONS

This section describes the relationship between fluctuations in the velocity and thermodynamic fields. The impact of supersaturation fluctuations on particle microphysics is also discussed.

The forcing of the velocity field is done to sustain flow turbulence and maintain finite amplitude of fluctuations in the otherwise zero-mean-velocity flow fields in homogeneous and isotropic turbulence. The time evolutions of the root-mean-square (rms) of the velocity fields (u_{rms}) are shown in Fig. 21(a) (Study I) and Fig. 21(b) (Study II) for different turbulence levels but the same (lognormal) dry aerosol size distribution. The u_{rms} goes through some transient period before reaching a statistically stationary state after approximately 6 s, with the details depending on the levels of turbulence.

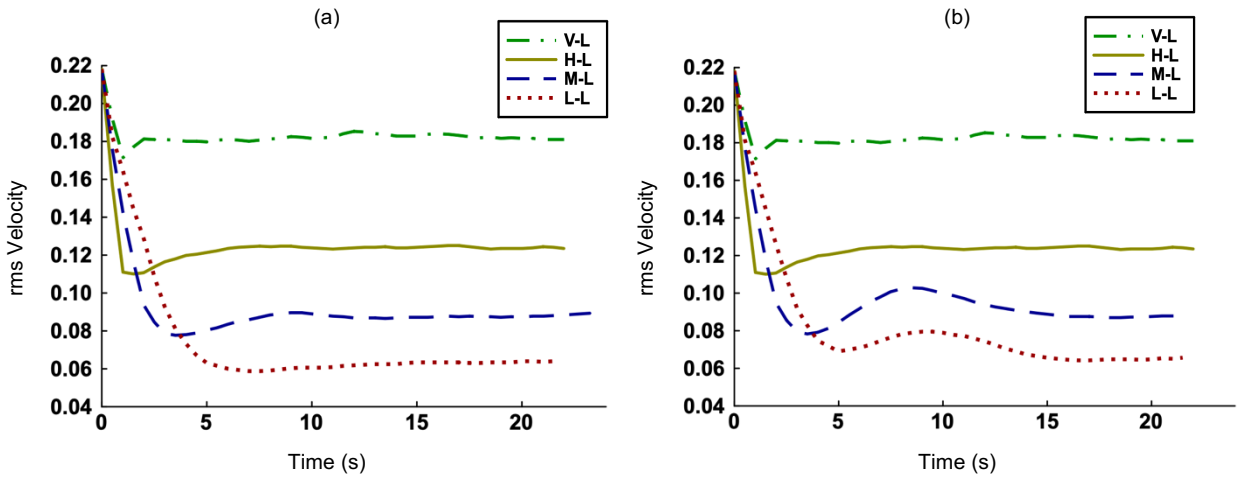

FIG. 21 Time evolution of the rms velocities in (a) Study I, and (b) Study II. 'V', 'H', 'M', and 'L' before dash (-) stand for 'very high', 'high', 'medium', and 'low' turbulence levels.

Figures 22(a)-(c) show the PDFs of fluctuating z-velocity, temperature, and vapor mixing ratio, respectively. These graphs represent Study I at 10 s. The PDFs of fluctuating temperature and vapor mixing ratio in Study II at 10 s are plotted in Figs. 22(d)-(e). We see in Fig. 22(a) that higher turbulence intensities broaden the distributions of the fluctuating z-velocity (w'), with significantly larger standard deviations from the mean, which is zero in this problem. The PDFs of the fluctuating x- and y-velocities are found to be similar, as expected from homogeneity and isotropy. However, the PDFs of the fluctuating thermodynamic fields are narrower for Cases V-L and H-L compared to those for Cases M-L and L-L in both Study I (Figs. 22(b)-(c)) and Study II (Figs. 22(d)-(e)). This suggests that fluctuations, or deviations from the means, in the thermodynamic fields decrease with increasing flow turbulence intensity. Higher flow turbulence enhances mixing ($\rho\langle u_i'(\boldsymbol{x},t)\theta\rangle$), where θ is a placeholder for temperature and vapor mixing ratio, and the angular brackets, $\langle . \rangle$, indicate spatial averaging. Stronger mixing causes fluctuations in the thermodynamic fields to spread out. Thus, passive thermodynamic fields[44] are more homogenized because of higher flow turbulence level.

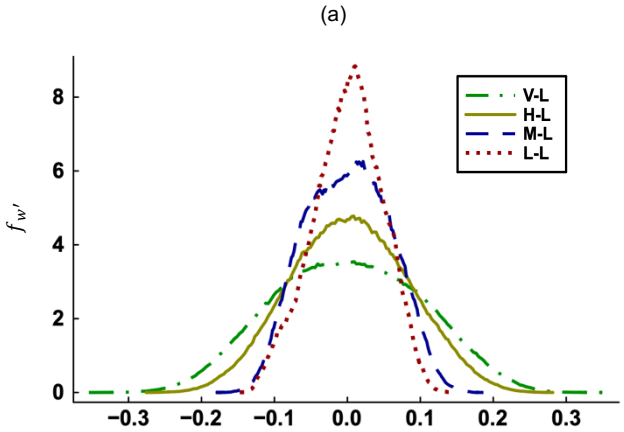

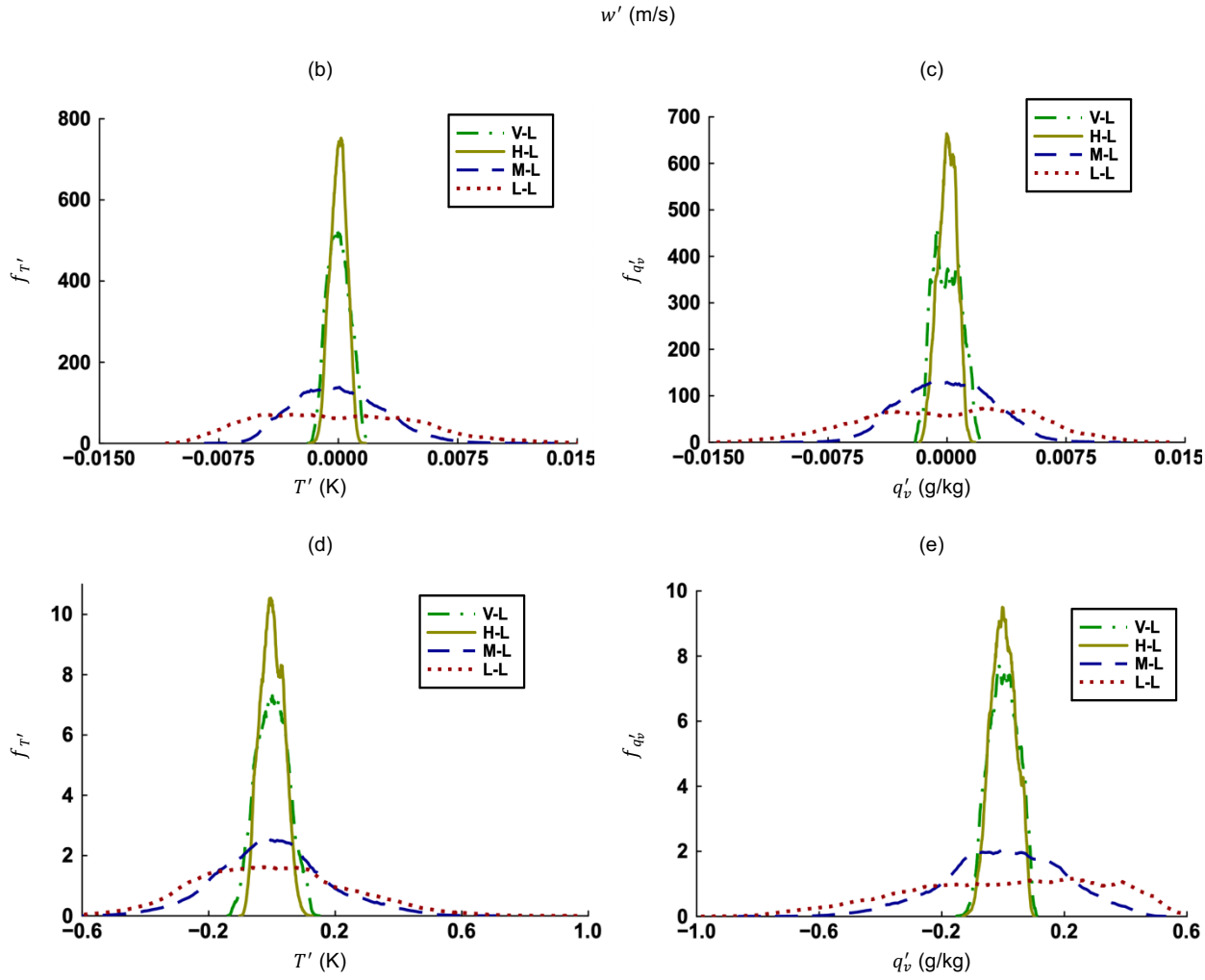

FIG. 22 PDFs of (a) fluctuating z-velocity (w'), (b) fluctuating temperature (T'), and (c) fluctuating vapor mixing ratio (q_v'), in Study I at 10 s. PDFs of fluctuating (d) temperature and (e) vapor mixing ratio, in Study II at 10 s. 'V', 'H', 'M', and 'L' before dash (-) stand for 'very high', 'high', 'medium', and 'low' turbulence levels.

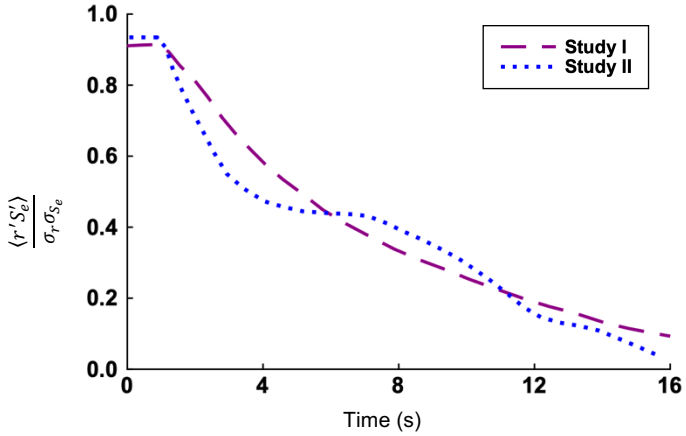

FIG. 23 Time evolution of the correlation coefficient $\langle r'S_e' \rangle / \sigma_r \sigma_{S_e}$ for Case L-L in Studies I and II.

To understand the connection between fluctuations in the environmental supersaturation and particle radius, we show the time evolution of the correlation coefficient $\langle r' S_e' \rangle / \sigma_r \sigma_{S_e}$ in Fig. 23. The r' is strongly correlated with the S_e' at earlier times but the correlation decays over time as expected in homogeneous turbulence. We observe that the $\langle r' S_e' \rangle / \sigma_r \sigma_{S_e}$ and thus the $\langle r' S_e' \rangle$ are positive throughout the simulations. Therefore, positive and negative fluctuations in the supersaturation cause positive and negative fluctuations in the particle radius, respectively. Hence, the S_e' always broaden the spread of particle radii (σ_r).

A. CONCLUDING REMARKS

The activation of aerosol particles and deactivation of cloud droplets in turbulent atmosphere are numerically investigated by use of a finite difference-based direct numerical simulation (DNS) model. A spatially three-dimensional model in the core of atmospheric cloud is analyzed, and the combined effects of curvature and solute are investigated, as are the effects of turbulence intensity and the initial distribution of particles (monodisperse and polydisperse). The major results are summarized as follows:

- Air temperature increases while vapor mixing ratio and supersaturation decrease faster when curvature and solute effects are included (Figs. 5(a)-(c)), resulting in weaker condensation. The initial dry aerosol size distribution (monodisperse or lognormal) does not appear to affect the magnitude and temporal evolution of air temperature, supersaturation, and vapor mixing ratio (Figs. 5(a)-(c)).
- For the same (high) turbulence intensity and monodisperse dry size distribution, activation is more rapid when curvature and solute effects are not included in the model (Case H in Fig. 6(a)). The mean particle radius is also larger for this case (Fig. 6(c)). For the same (high) turbulence intensity, activation takes place more rapidly in our study when the initial size distribution of aerosol is monodisperse (Case H-M) compared to lognormal (Case H-L).
- With the lognormal initial dry size distribution, there is an overlap in the size distributions of aerosol particles and cloud droplets at short and medium time during simulation. That is, we can have a small particle classified as cloud droplet and a larger one as an aerosol particle. Also, larger aerosol particles in a lognormal distribution take more time to activate into cloud droplets compared to the smaller particles. The results are consistent with the kinetic effects discussed in literature.[45]

- For the cases of deactivation and high turbulence (H, H-M, H-L), neither the presence of dry aerosol (solute) nor its size distribution has any significant effects on air temperature, vapor mixing ratio, and supersaturation (Figs. 9(a)-(c)). The numbers of deactivated cloud droplets are also identical for the three cases (Fig. 10(a)).
- We have a temporal reduction in radius (Fig. 10(b)) as cloud droplets deactivate and evaporate. As the droplet radius decreases, curvature and solute effects start to become significant.
- Turbulence appears to delay activation (Fig. 15(a)). The higher the turbulence intensity, the smaller the droplet radius (Fig. 15 (b)) and the narrower the PDFs of droplet radius. But turbulence appears to promote deactivation (Fig. 19(a)) as the number of deactivated cloud droplets is higher with increasing turbulence intensity. The mean radius of aerosol particles (from deactivated cloud droplets) is larger when turbulence intensity is higher (Fig. 19(b)).
- Activation appears to be mean-dominated in Study I (Fig. 14) although with a small probability of fluctuation-influenced activation or deactivation at early time. Deactivation is mean-dominated in Study II (Fig. 18), but also with a small probability of fluctuation-influenced activation or deactivation. Prabhakaran et al.[12] reported on mean-dominated and fluctuation-influenced regimes from simplified one-dimensional theoretical treatment and physical experiments. Our approach is based on full three-dimensional DNS modeling.
- Stronger turbulence leads to increased homogenization of the passive thermodynamic fields (Figs. 22(b)-(e)) in our study. Hence, the smaller variance of environmental supersaturation is associated with higher turbulence intensities (Figs. 13(b) and 17(b)). Vaillancourt et al.[46] also reported that fluctuations in supersaturation decrease when the turbulence intensity increases, even though their domain length in each spatial coordinate direction is one-fifth of the one used in the present study (0.10 m versus 0.512 m).
- Bimodality is observed in the radius PDFs of aerosol particles during deactivation (Fig. 12). The radius PDFs of cloud droplets broaden at early times but narrow at later times (Figs. 7, 8, 11, 12) in both studies.

It is noteworthy that the present study is focused on the influence of turbulence only through external momentum forcing, with the impact of external thermodynamic forcing being ignored. Our future study will consider external thermodynamic forcing, wherein the competition between turbulent homogenization and source of thermodynamic variance is expected.

ACKNOWLEDGEMENTS

This research used resources of the National Energy Research Scientific Computing Center (NERSC), a Department of Energy Office of Science User Facility using NERSC award NERSC ASCR-ERCAP0027399. We acknowledge support from the LDRD program at Brookhaven National Laboratory, which is sponsored by the US Department of Energy, Office of Science, under Contract Number DE-SC0012704. This project was partially funded by 2022 Stony Brook University (SBU) - Brookhaven National Laboratory (BNL) Seed Grant Program Award #: 94508.

APPENDIX A: SOME DETAILS ON TURBULENCE FORCING

To create the 'low' ,'medium', 'high', and 'very high' turbulence levels, we have applied forcing in the following wavenumber bands: $1 \leq k_f/k_{min} \leq 2.45$, $1 \leq k_f/k_{min} \leq 4.12$, $1 \leq k_f/k_{min} \leq 8.12$, and $1 \leq k_f/k_{min} \leq 17.32$, respectively, where k_f is the forced wavenumber, and $k_{min} = 2\pi/L = 12.27$ is the minimum wavenumber using $L = 0.512\ m$. The maximum wavenumber is $k_{max} = N\pi/L = 1570.8$ using $N = 256$. Note that $k_{max} \sim 128 k_{min}$. The ratios of k_{max} to the largest k_f are 52.24, 31.07, 15.76, and 7.39, respectively. Eswaran and Pope[18] used $2\sqrt{2}k_{min}$ as the largest k_f in a 64^3 simulation, with $k_{max} \sim 30.17 k_{min}$ and a ratio of k_{max} to largest k_f of 10.67. Therefore, the forced wavenumber bands in our model are narrower than that in Ref. 18 except for the case of very high turbulence level. According to Eq. (4), variation of either ϵ_{in} or the wavenumber band should produce different turbulence intensities. But we have observed that ϵ_{in} does not have a significant impact in this regard. We ran four test cases that differ in either ϵ_{in}, the wavenumber band, or both. The ϵ_{in} was varied from 0.004 m^2/s^3 to 0.016 m^2/s^3, while the wavenumber band was varied from $1 \leq k_f/k_{min} \leq 4.12$ to $1 \leq k_f/k_{min} \leq 8.12$. Figure 24(a) shows that the TKE dissipation rate increases only marginally with increasing ϵ_{in}, but significantly with changes in the wavenumber band. Figure 24(b) suggests that the four spectra converge at intermediate and small scales while being different at large scales, as expected. Hence, the different results discussed in Sec. IV B can be attributed to differences in k_f.

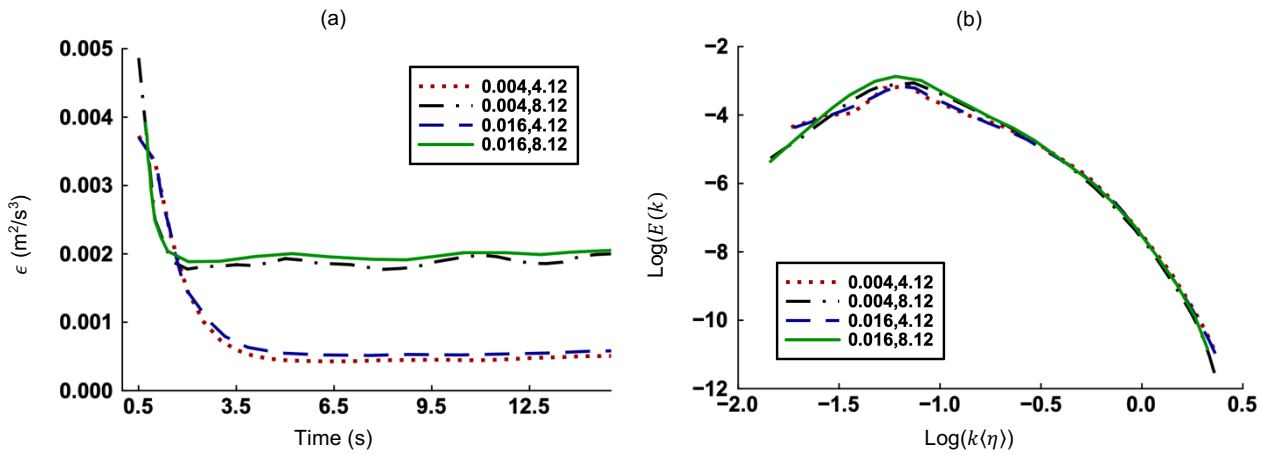

FIG. 24 (a) Time evolution of TKE dissipation rate (ϵ), and (b) TKE spectra at 6 s in log format, for the four cases. Note that wavenumbers (k) in the abscissa are multiples of k_{min} and are in the radial coordinate direction. In the legends, the value of ϵ_{in} (m^2/s^3) and the maximum forcing wavenumber are separated by a comma.

The initial velocity field has been constructed in the Fourier space[47] to satisfy continuity, isotropy, and homogeneity with a given energy spectrum. A regular cubic grid of points, each of which supports a single Fourier mode,[18] is employed in the Fourier space. The initial TKE spectrum from the velocity is specified as[48]

$$E(k) = \frac{16}{\sqrt{\pi/2}} \frac{u_0^2 k^4}{k_0^5} \exp\left(-\frac{2k^2}{k_0^2}\right), \tag{33}$$

where $k_0 = 2.45k_{min}$ and $u_0 = 0.22\ m/s$ is the rms velocity from the generated fluctuating velocity field. The form k^4 for low wavenumbers correspond to the incompressible limit while the exponential function allows a rapid roll-off of the energy at high wavenumbers.

Of interest in our analysis is the integral length scale, l, which is calculated as[49]

$$l = \int_0^\infty R_{w'w'}(\boldsymbol{r}) dr\,, \tag{34}$$

The autocorrelation coefficient, $R_{w'w'}$, is defined as[44]

$$R_{w'w'}(\boldsymbol{r}) = \frac{\langle w'(\boldsymbol{x},t) w'(\boldsymbol{x}+\boldsymbol{r},t)\rangle}{\sqrt{\langle \left(w'(\boldsymbol{x},t)\right)^2\rangle \langle \left(w'(\boldsymbol{x},t)\right)^2\rangle}}\,, \qquad \boldsymbol{r} = \Delta x\boldsymbol{i} + \Delta y\boldsymbol{j} + \Delta z\boldsymbol{k}\,. \tag{35}$$

where w' is the fluctuating z-velocity and $\boldsymbol{r}$ is the separation distance vector. The l can be interpreted as the separation distance in Fig. 25 at which the autocorrelation is approximately zero. The values of l using Fig. 25 are 0.18 m, 0.15 m, 0.12 m, and 0.10 m, respectively for 'low' ,'medium', 'high', and 'very high' turbulence level cases. With a domain length (L) of 0.512 m, the corresponding values of L/l are 2.84, 3.41, 4.27, and 5.12. We are aware of suggestions that the typical l should be one-eighth[51] of the domain size (L). However, these are based on scaling arguments and

not exact relationships. The box length is sufficiently larger than the integral length scales for our purpose. Note that previous studies by Pope and his coworkers were not able to use an L/l of 8 but rather assumed values of approximately 4.5[50] and 3.0.[18]

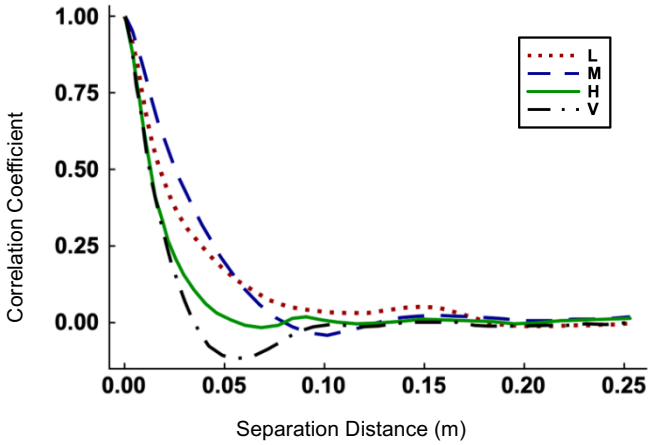

FIG. 25 The autocorrelation coefficients for z-velocity at 6 s. 'L', 'M', 'H', and 'V' stand for 'low', 'medium', 'high', and 'very high' turbulence levels.

DATA AVAILABILITY

The data that support the findings of this work are available from the corresponding author upon reasonable request.

[1]J. Ovadnevaite, A. Zuend, A. Laaksonen, K.J. Sanchez, G. Roberts, D. Ceburnis, S. Decesari, M. Rinaldi, N. Hodas, M.C. Facchini, and J.H. Seinfeld, "Surface tension prevails over solute effect in organic-influenced cloud droplet activation," *Nature*, *546*(7660), 637-641 (2017).

[2]Z. Li, A.L. Williams, and M.J. Rood, "Influence of soluble surfactant properties on the activation of aerosol particles containing inorganic solute," *Journal of the atmospheric sciences*, *55*(10), pp.1859-1866 (1998).

[3]F. Yang, P. Kollias, R.A. Shaw, and A.M. Vogelmann, "Cloud droplet size distribution broadening during diffusional growth: ripening amplified by deactivation and reactivation," *Atmospheric Chemistry and Physics*, *18*(10), 7313-7328 (2018).

[4]F. Yang, R.A. Shaw, M. Ovchinnikov, and A.M. Vogelmann, "An intercomparison of large-eddy simulations of a convection cloud chamber using haze-capable bin and Lagrangian cloud microphysics schemes," *Journal of Advances in Modeling Earth Systems*, *15*(5), p.e2022MS003270 (2023).

[5]A.V. Korolev, "The influence of supersaturation fluctuations on droplet size spectra formation," *Journal of the atmospheric sciences*, *52*(20), pp.3620-3634 (1995).

[6]R.A. Shaw, "Particle-turbulence interactions in atmospheric clouds," *Annual Review of Fluid Mechanics*, *35*(1), pp.183-227 (2003).

[7]W.W. Grabowski, L. Thomas, and B. Kumar, "Impact of cloud-base turbulence on CCN activation: single-size CCN," *Journal of the Atmospheric Sciences*, *79*(2), 551-566 (2022).

[8]A.S.M. Shawon, P. Prabhakaran, G. Kinney, R.A. Shaw and W. Cantrell, "Dependence of Aerosol-Droplet Partitioning on Turbulence in a Laboratory Cloud," *Journal of Geophysical Research: Atmospheres*, *126*(5), e2020JD033799 (2021).

[9]A. Celani, A. Mazzino, and M. Tizzi, "The equivalent size of cloud condensation nuclei," *New Journal of Physics*, *10*(7), p.075021 (2008).

[10]F. Ditas, R.A. Shaw, H. Siebert, M. Simmel, B. Wehner and A. Wiedensohler, "Aerosols-cloud microphysics-thermodynamics-turbulence: evaluating supersaturation in a marine stratocumulus cloud," *Atmospheric Chemistry and Physics*, *12*(5), 2459-2468 (2012).

[11]L. Thomas, B. Kumar, A. Zuend, D. Hassan-Barthaux and S.A. Rao, "CCN activation in homogeneous isotropic turbulence: Response to particle characteristics and environmental conditions," *Atmospheric Research*, *297*, 107095 (2024).

[12]P. Prabhakaran, A.S.M. Shawon, G. Kinney, S. Thomas, W. Cantrell, and R.A. Shaw, "The role of turbulent fluctuations in aerosol activation and cloud formation," *Proceedings of the National Academy of Sciences*, *117*(29), pp.16831-16838 (2020).

[13]S.B. Pope, "Ten questions concerning the large-eddy simulation of turbulent flows," *New journal of Physics*, *6*(1), 35 (2004).

[14]Z. Gao, Y. Liu, X. Li, and C. Lu, "Investigation of turbulent entrainment-mixing processes with a new particle-resolved direct numerical simulation model," *Journal of Geophysical Research: Atmospheres*, *123*(4), 2194-2214 (2018).

[15]M.D. Petters, and S.M. Kreidenweis, "A single parameter representation of hygroscopic growth and cloud condensation nucleus activity," *Atmospheric Chemistry and Physics*, *7*(8), 1961-1971 (2007).

[16]M. Andrejczuk, W.W. Grabowski, S.P. Malinowski, and P.K. Smolarkiewicz, "Numerical simulation of cloud–clear air interfacial mixing," *Journal of the atmospheric sciences*, *61*(14), 1726-1739 (2004).

[17]D. Carati, S. Ghosal, and P. Moin, "On the representation of backscatter in dynamic localization models," *Physics of Fluids*, *7*(3), 606-616 (1995).

[18]V. Eswaran and S.B. Pope, "An examination of forcing in direct numerical simulations of turbulence," *Computers & Fluids*, *16*(3), 257-278 (1988).

[19]P. Vaillancourt, "Microscopic approach to cloud droplet growth by condensation," Ph.D. Thesis, McGill University, Montreal, Quebec, 1998.

[20]B. Kumar, J. Schumacher, and R.A. Shaw, "Lagrangian mixing dynamics at the cloudy–clear air interface," *Journal of the Atmospheric Sciences*, *71*(7), pp.2564-2580 (2014).

[21]J.K. Eaton, and J. Fessler, "Preferential concentration of particles by turbulence," *International Journal of Multiphase Flow*, *20*, pp.169-209 (1994).

[22]H.R. Pruppacher and J.D. Klett, *Microphysics of clouds and precipitation: Reprinted 1980*. (Springer Science & Business Media, 2012).

[23]D. Newth, and D. Gunasekera, "Projected changes in wet-bulb globe temperature under alternative climate scenarios," *Atmosphere*, *9*(5), 187 (2018).

[24]J. Huang, "A simple accurate formula for calculating saturation vapor pressure of water and ice," *Journal of Applied Meteorology and Climatology*, *57*(6), 1265-1272 (2018).

[25]P. C. Zieger, "Effects of relative humidity on aerosol light scattering," Ph.D. Thesis, ETH Zurich, Zurich, 2011.

[26]R. West, *The parameterisation of microphysical cloud droplet formation in the Met Office Unified Model* (2009).

[27]D. D. A. Rothenberg, "Fundamental aerosol-cloud interactions and their influence on the aerosol indirect effect on climate," Ph.D. Thesis, Massachusetts Institute of Technology, Boston, 2017.

[28]H. Abdul-Razzak, S.J. Ghan, and C. Rivera-Carpio, "A parameterization of aerosol activation: 1. Single aerosol type," *Journal of Geophysical Research: Atmospheres*, *103*(D6), pp.6123-6131 (1998).

[29]H. Tennekes, and J.L. Lumley, *A first course in turbulence* (MIT press, Massachusetts, 1972).

[30]H. Siebert, R.A. Shaw, and Z. Warhaft, "Statistics of small-scale velocity fluctuations and internal intermittency in marine stratocumulus clouds," *Journal of the atmospheric sciences*, *67*(1), 262-273 (2010).

[31]D. Rose, S.S. Gunthe, E. Mikhailov, G.P. Frank, U. Dusek, M.O. Andreae, and U. Pöschl, "Calibration and measurement uncertainties of a continuous-flow cloud condensation nuclei counter (DMT-CCNC): CCN activation of ammonium sulfate and sodium chloride aerosol particles in theory and experiment," *Atmospheric Chemistry and Physics*, *8*(5), 1153-1179 (2008).

[32]J. Glimm, J. W. Grove, X.L. Li, K.M. Shyue, Y. Zeng, and Q. Zhang, "Three-dimensional front tracking," *SIAM Journal on Scientific Computing*, *19*(3), 703-727 (1998).

[33]S. Balay, S. Abhyankar, M. Adams, J. Brown, P. Brune, K. Buschelman, L. Dalcin, A. Dener, V. Eijkhout, W. Gropp and, D. Karpeyev, "PETSc users manual," (2019).

[34]T. Gotoh, D. Fukayama, and T. Nakano, "Velocity field statistics in homogeneous steady turbulence obtained using a high-resolution direct numerical simulation," *Physics of Fluids*, *14*(3), pp.1065-1081 (2002).

[35]V. Nair, T. Heus, and M. van Reeuwijk, "A Lagrangian study of interfaces at the edges of cumulus clouds," *Journal of the Atmospheric Sciences*, *78*(8), pp.2397-2412 (2021).

[36]R. Gallego, M. Castro, and J.M. López, "Pseudospectral versus finite-difference schemes in the numerical integration of stochastic models of surface growth," *Physical Review E—Statistical, Nonlinear, and Soft Matter Physics*, *76*(5), p.051121 (2007).

[37]R. Mittet, "On the pseudospectral method and spectral accuracy," *Geophysics*, *86*(3), pp.T127-T142 (2021).

[38]T. MacMillan, R.A. Shaw, W.H. Cantrell, and D.H. Richter, "Direct numerical simulation of turbulence and microphysics in the Pi Chamber," *Physical Review Fluids*, *7*(2), p.020501 (2022).

[39]W. Bo, X. Liu, J. Glimm, and X. Li, "A robust front tracking method: verification and application to simulation of the primary breakup of a liquid jet," *SIAM Journal on Scientific Computing*, *33*(4), 1505-1524 (2011).

[40]P.K. Wu, and G.M. Faeth, "Aerodynamic effects on primary breakup of turbulent liquids," *Atomization and Sprays*, *3*(3) (1993).

[41]J. Du, B. Fix, J. Glimm, X. Jia, X. Li, Y. Li, and, L. Wu, "A simple package for front tracking," *Journal of Computational Physics*, *213*(2), 613-628 (2006).

[42]W.W. Grabowski, and L.P. Wang, "Growth of cloud droplets in a turbulent environment," *Annual review of fluid mechanics*, *45*(1), pp.293-324 (2013).

[43]A.A.M. Sharfuddin, and F. Ladeinde, "Particle-Resolved Direct Numerical Simulation of Turbulence-Cloud-Aerosol Interactions," AIAA Paper No. 2024-2562, 2024.

[44]F. Ladeinde and, H. Oh, "Stochastic and spectra contents of detonation initiated by compressible turbulence thermodynamic fluctuation," *Physics of Fluids 33, 045111* (2021).

[45]J. Chen, Y. Liu, M. Zhang, and Y. Peng, "Height dependency of aerosol-cloud interaction regimes," *Journal of Geophysical Research: Atmospheres*, *123*(1), pp.491-506 (2018).

[46]P.A. Vaillancourt, M.K. Yau, P. Bartello, and W.W. Grabowski, "Microscopic approach to cloud droplet growth by condensation. Part II: Turbulence, clustering, and condensational growth," *Journal of the atmospheric sciences*, *59*(24), pp.3421-3435 (2002).

[47]R.S. Rogallo, "Numerical experiments in homogeneous turbulence," *National Aeronautics and Space Administration* (Vol. 81315, 1981).

[48]C. Rosales, and C. Meneveau, "Linear forcing in numerical simulations of isotropic turbulence: Physical space implementations and convergence properties," *Physics of fluids*, *17*(9) (2005).

[49]S.B. Pope, *Turbulent flows* (Cambridge University Press, Cambridge, 2000).

[50]M.R. Overholt, and S.B. Pope, "Direct numerical simulation of a passive scalar with imposed mean gradient in isotropic turbulence," *Physics of Fluids*, *8*(11), pp.3128-3148 (1996).